

PARAMETRIC AERODYNAMIC STUDY OF LEADING-EDGE SERRATIONS ON WING SECTIONS ACROSS REYNOLDS NUMBERS

Jordan J. Whittaker[1]

[1]University of New South Wales, Sydney, NSW 2052, Australia

Abstract

Sinusoidal leading-edge serrations are investigated as passive stall-control devices on a cambered NACA 2412 wing section. Serration wavelength, amplitude, and termination distance are parameterised relative to the average chord of an aspect-ratio-two wing section and evaluated at Reynolds numbers of 100,000 and 500,000. An automated large-eddy simulation workflow in ANSYS Fluent is used for the parametric sweep, with selected low-Reynolds-number cases compared experimentally in the UNSW Educational Wind Tunnel. Performance is assessed across representative pre-stall, stall, and post-stall regimes using lift, drag, and lift-to-drag ratio. Smaller, less perturbing serrations are generally favoured before stall, whereas larger amplitudes provide the clearest post-stall benefit. At a Reynolds number of 100,000, the configuration with wavelength 1/6.5, amplitude 0.03, and termination distance 0.35, each relative to the average chord, provides one of the strongest cross-regime compromises, remaining within 8 percent of the nominal maximum normalised lift-to-drag ratio at all three operating points. At a Reynolds number of 500,000, preferred configurations vary more strongly with stall regime, and the low-Reynolds-number compromise does not transfer directly. The nominal optima shift from wavelength-to-amplitude ratios of approximately 10 to 20 before and near stall to approximately 3.3 after stall, although a shared band of approximately 4 to 8 contains regime-specific configurations within 5 percent of the nominal maximum at all six operating points. Termination distance is secondary to wavelength and amplitude within the tested space. The resulting data and performance maps provide a practical starting point for industry-led, application-specific design, while recognising that performance remains sensitive to wing geometry, Reynolds number, and operating regime. Overall, leading-edge serrations are best interpreted as regime-dependent stall-management devices rather than general efficiency-enhancement devices.

Keywords: leading-edge serrations, stall, large-eddy simulation (LES), parametric study, aerodynamics

1. Introduction

Leading-edge (LE) serrations, or tubercles, are passive geometric modifications formed by periodic protrusions along the leading edge of a lifting surface. They are most commonly studied in a sinusoidal or quasi-sinusoidal form, following the tubercles found on the pectoral flippers of humpback whales. The biological motivation is useful because it identifies a naturally occurring high-angle-of-attack lifting surface, but the engineering interest is more specific: LE serrations can modify separation behaviour, particularly near stall and in the post-stall regime [1–5]. For aircraft, wind-turbine sections, rotor blades, hydrofoils, and small unmanned aircraft, this makes them relevant where the flow is expected to operate away from a purely attached, low-incidence condition.

The main aerodynamic behaviour reported in the literature is not a universal improvement in performance, but a change in the way the lifting surface enters and passes through stall. Early experimental studies showed that tubercled leading edges can soften the stall response, replacing the sharper loss of lift seen on the baseline airfoil with a more gradual post-stall decay [2–5]. This behaviour often improves post-stall lift or lift-to-drag ratio, C_L/C_D, and can reduce the severity of stall onset. However, the same modifications can also introduce pre-stall penalties through increased drag, reduced

https://doi.org/10.71945/icas2026_0723

attached-flow lift, or reduced maximum lift coefficient, depending on the geometry and operating conditions [3, 5–8]. For this reason, LE serrations are better treated as regime-dependent stall-control devices than as general lift-enhancement devices.

A common physical interpretation in the literature is that serrations modify separated flow through streamwise or counter-rotating vortical structures generated near the serration peaks and troughs. These structures have been reported to redistribute momentum, modify local separation, and create separated pressure regions over parts of the span [9–11]. This interpretation is particularly relevant in separated and partially separated flow, where changes in local separation behaviour can produce large changes in the force coefficients. However, the mechanism should not be stated too narrowly. At low Reynolds number, Re, laminar separation bubble behaviour can be important, while finite-wing effects, spanwise flow redistribution, trough separation, transition behaviour, and airfoil-specific pressure gradients also influence the response [12–15]. The aerodynamic response is therefore linked to geometry, Re, and angle of attack, α, rather than to the presence of serrations alone.

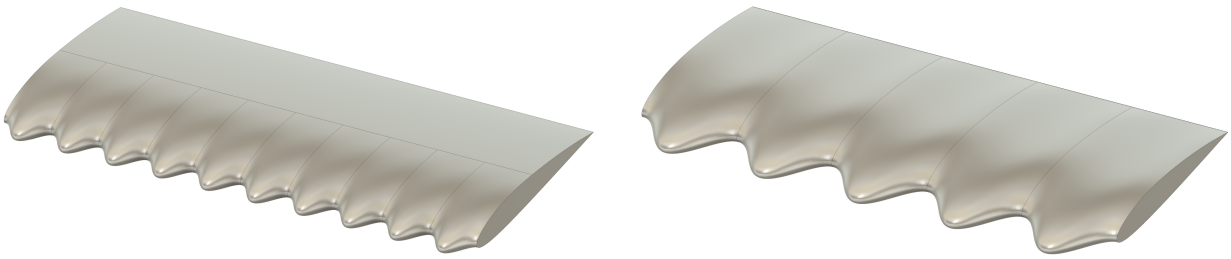
Previous work has shown that wavelength, W, and amplitude, A, are the primary geometric variables controlling serration behaviour. Studies by Johari et al., Hansen, Favier et al., Stalnov and Chong, and Lacagnina et al. show that changing the amplitude and wavelength can shift both the magnitude and the regime in which performance benefits occur [3, 5, 7–9]. A wavelength-to-amplitude ratio has been used to interpret some of these trends, with favourable configurations often occurring within a moderate ratio range rather than at the extremes of either parameter [7, 8]. However, this ratio does not provide a universal collapse of the data. Very small serrations may perturb the attached flow without producing a sufficient stall-control benefit, while large serrations may improve post-stall behaviour but impose stronger drag or stall-regime penalties.

Such broader literature also shows that the same serration geometry cannot be assumed to transfer directly between airfoils, Reynolds numbers, and planforms. Hansen and others showed that airfoil profile can change the effectiveness of tubercles, while Fernandes et al. provide one of the more directly relevant precedents for a cambered NACA 2412-based investigation [4–6]. Finite-wing and application-specific studies further show that the effect of LE serrations depends on aspect ratio, tip effects, operating environment, and the chosen performance metric [16–18]. Reynolds-number dependence is also not resolved by a single trend. Recent work indicates that changing Re can alter the baseline separation process, transition behaviour, and the location of high-performing geometry bands [13–15]. This is particularly important for low- to moderate-Re applications, where laminar separation and transition effects can be sensitive to relatively small changes in geometry.

Several parametric studies have already contributed to this understanding. Favier et al. numerically examined wavy leading edges in separated flow and connected geometry to flow-control behaviour [9]. Stalnov and Chong considered scaling of lift behaviour with LE serration geometry [8]. Lacagnina et al. investigated leading-edge serrations across low-angle-of-attack, pre-stall, and post-stall conditions, giving one of the more useful experimental comparisons of geometry and regime dependence [7]. Other studies have extended the problem to different airfoils, wind-turbine sections, UAV wings, finite wings, aeroacoustic trade-offs, and turbulence-model sensitivity [14, 15, 18, 19]. These studies establish the main physical and aerodynamic trends, but they also show why cross-study comparison is difficult. The parameter ranges, airfoils, Reynolds numbers, serration profiles, termination methods, turbulence models, and performance metrics are rarely controlled together.

One geometric variable that remains much less systematically treated than wavelength and amplitude is the termination distance, T, or insertion length, of the serration into the airfoil. Many studies use either a full-chord modification, an insertion of approximately one-third chord, or a fixed geometry, without isolating the effect of termination distance. This matters because termination distance controls how abruptly the serrated leading-edge geometry returns to the unmodified airfoil, and therefore affects the local pressure distribution, chordwise geometry transition, and separated-flow behaviour near the leading edge. A controlled study of termination distance is therefore needed alongside the more commonly studied wavelength and amplitude parameters.

This paper extends the previous $Re = 1 \times 10^5$ study by Whittaker and Doolan [20]. The published low-Re dataset is reanalysed with regenerated figures and revised uncertainty treatment, then combined with new $Re = 5 \times 10^5$ simulations. A controlled sweep of wavelength, amplitude, and termination



(a) (b)

Figure 1 – Representative serrated wing-section geometries: (a) $[1/5, 0.05, 0.5]_{\mathrm{SC}}$ and (b) $[1/2.5, 0.1, 1.0]_{\mathrm{SC}}$.

distance is applied to a cambered NACA 2412 wing section while planform area is held constant; representative geometries are shown in Figure 1. The study uses an automated large-eddy simulation workflow in ANSYS Fluent, supported by experimental trend verification in the UNSW Educational Wind Tunnel. Rather than seeking a universal optimum or resolving every flow mechanism, it maps geometry-dependent performance across pre-stall, stall, and post-stall conditions and tests whether w/a provides useful guidance across the two Reynolds numbers.

The paper is structured as follows. Section 2 defines the serrated wing-section geometry, parameter space, computational setup, and experimental verification method. Section 3 presents the aerodynamic trends in wavelength and amplitude at both Reynolds numbers, followed by the effects of termination distance and cross-Reynolds-number design implications. Section 4 summarises the main conclusions on the use of LE serrations as regime-dependent passive stall-control devices.

2. Methodology

2.1 Serrated wing-section geometry

The serrated wing sections were generated from a cambered NACA 2412 airfoil with an average chord of $C = 100$ mm and a span of $S = 200$ mm, giving an aspect ratio of $AR = 2$. The geometry was selected to represent a finite wing section rather than an infinite two-dimensional airfoil, while remaining small enough for consistent manufacturing and experimental verification in the available wind tunnel. The NACA 2412 profile was also chosen to keep the study relevant to a general cambered aircraft wing section, rather than to a symmetric airfoil or a specialised biological profile.

The leading-edge (LE) serrations were defined by a sinusoidal variation in chord along the spanwise coordinate, x. The three geometric properties of interest were the serration wavelength, W, amplitude, A, and termination distance, T. These were nondimensionalised by the average chord as:

$$w = \frac{W}{C}, \qquad a = \frac{A}{C}, \qquad t = \frac{T}{C}. \tag{1}$$

The variable chord profile was defined as:

$$c(x) = C - A\cos\left(\frac{2\pi x}{W}\right). \tag{2}$$

The termination distance, T, defines the chordwise portion of the airfoil that is scaled to match the local chord profile in Eq. 2. For example, $t = 1$ corresponds to a fully inserted serration, in which the entire airfoil section is scaled by $C(x)$, whereas smaller values of t confine the geometric perturbation closer to the leading edge. The aerodynamic coefficients used the fixed reference area $S_{\mathrm{ref}} = 0.020$ m^2. Pitching moment was referenced to the quarter-chord, with positive C_M denoting nose-up.

The wavelengths were selected as integer divisions of the span, ensuring that the geometry remained symmetric about the centre chord. Depending on the wavelength, the centreline therefore coincides with either a serration peak or trough. This avoids asymmetric loading caused by incomplete serration periods and allows the same spanwise extent to be used across all geometries. Figure 2 defines the

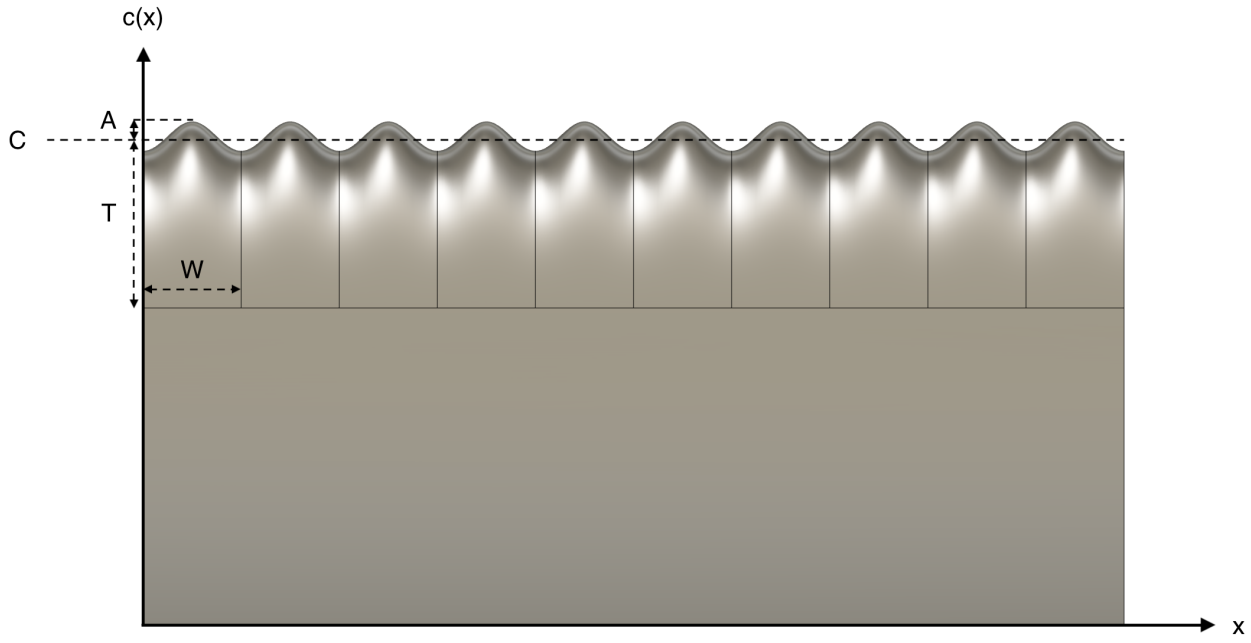


Figure 2 – Serration-parameter schematic showing A, W, T, C, and $c(x)$.

geometric parameters, and Figure 1 shows representative serrated wing-section models across the parameter range.

2.2 Parameter space

The geometric parameter space was defined using the following nondimensional wavelength, amplitude, and termination-distance values:

$$w = \frac{W}{C} = \left[\frac{1}{50}, \frac{1}{28.5}, \frac{1}{20}, \frac{1}{13.5}, \frac{1}{10}, \frac{1}{6.5}, \frac{1}{5}, \frac{1}{4}, \frac{1}{3.5}, \frac{1}{3}, \frac{1}{2.5}, \frac{1}{2}\right], \tag{3}$$

$$a = \frac{A}{C} = [0.0025,\ 0.005,\ 0.01,\ 0.015,\ 0.02,\ 0.025,\ 0.03,\ 0.04,\ 0.05,\ 0.075,\ 0.1,\ 0.15], \tag{4}$$

$$t = \frac{T}{C} = [0.1,\ 0.2,\ 0.35,\ 0.5,\ 0.75,\ 1.0]. \tag{5}$$

The main wavelength–amplitude sweep was conducted at $t = 0.35$. This value was selected as a representative partial-insertion case, allowing direct comparison with a common termination distance used in the literature while avoiding the geometric severity of fully inserted serrations. The effect of termination distance was then investigated separately using a reduced set of wavelength–amplitude combinations. This separation kept the total simulation count feasible while still resolving the dominant wavelength–amplitude behaviour and the secondary sensitivity to t.

Not all formal combinations of Eqs. 3–5 were used. Geometries in which the termination distance was smaller than the amplitude were treated as incompatible, and additional combinations were omitted when the serration geometry became unrealistic or unsuitable for the mesh, model scale, or result quality. The main $t = 0.35$ sweep contained 130 retained serrated geometries at $Re = 1 \times 10^5$, with complete results retained for 127 of these geometries at $Re = 5 \times 10^5$. The termination-distance investigation comprised 17 tested $[w, a, t]_{\mathrm{SC}}$ configurations. Three of these were $t = 0.35$ cases already included in the main sweep, giving 14 additional unique geometries. The data-collection set therefore contained 144 unique serrated geometries, or 145 wing geometries when the unserrated baseline is included. Additional baseline and verification cases were simulated where required for normalisation, stall-regime selection, and experimental comparison.

Two Reynolds numbers were considered: $Re = 1 \times 10^5$ and $Re = 5 \times 10^5$. Using $C = 100$ mm and standard sea-level air properties, these correspond to freestream velocities of approximately $V_L =$

$14.61\ \mathrm{m\,s^{-1}}$ and $V_H = 73.04\ \mathrm{m\,s^{-1}}$, respectively. Rather than resolving the full stall distribution for every serration geometry, representative angles of attack were selected to describe the pre-stall, stall, and post-stall regimes. For the low-Reynolds-number case, the selected angles were $\alpha = 16^\circ$, 20°, and 25°. For the high-Reynolds-number case, the selected angles were $\alpha = 23^\circ$, 29°, and 34°. These angles were chosen from preliminary stall profiles of the baseline and representative serrated wing sections.

The main wavelength–amplitude sweep comprised 130 geometries for $Re = 1 \times 10^5$ with 127 of these geometries used at $Re = 5 \times 10^5$. The three missing high-Reynolds-number cases were lost because of cluster-node failures and were not rerun because neighbouring configurations in the same low-performing region had already established the local aerodynamic trend. These geometries were simulated at three angles of attack, giving 771 serrated data-collection simulations. The termination-distance profiles comprised 218 simulations, of which 18 $t = 0.35$ cases duplicated simulations already included in the main sweep. The complete dataset therefore contained 971 unique serrated data-collection simulations, excluding baseline cases and preliminary simulations used for setup development, mesh and domain assessment, and experimental verification.

Table 1 – Geometry and parameter-space summary.

Quantity	Symbol	Value
Airfoil profile	–	NACA 2412
Average chord	C	$100\ \mathrm{mm}$
Span	S	$200\ \mathrm{mm}$
Aspect ratio	AR	2
Serration form	–	Sinusoidal leading-edge serrations
Wavelength	$w = W/C$	Eq. 3
Amplitude	$a = A/C$	Eq. 4
Termination distance	$t = T/C$	Eq. 5
Main sweep	–	130 low-Re; 127 high-Re geometries
Termination sweep	–	14 additional geometries
Reynolds numbers	Re	1×10^5, 5×10^5
Freestream velocities	V	14.61, $73.04\ \mathrm{m\,s^{-1}}$
Low-Re angles of attack	α	16°, 20°, 25°
High-Re angles of attack	α	23°, 29°, 34°
Data-collection simulations	–	971

2.3 Computational method

The computational workflow was developed in ANSYS Workbench and ANSYS Fluent and automated in Python to support the large parameter sweep. Geometry files were generated from the parameterised model and then processed through a scripted workflow that copied a base simulation, assigned case-specific inputs, generated Workbench and Fluent journal files, and submitted jobs to high-performance computing clusters. The workflow was run on the UNSW Katana cluster and the National Computational Infrastructure GADI cluster. Katana was used extensively for setup development and preliminary simulations, while GADI was used for much of the final data collection. The automation reduced the manual effort required for the 971-case unique serrated data-collection set and ensured that geometry, Reynolds number, angle of attack, and post-processing were handled consistently across the dataset.

The computational domain was defined relative to the quarter-chord centre of the wing section. The final domain extended $\pm 5C$ in the vertical direction, $4C$ upstream, $12C$ downstream, and $\pm 2.5C$ in the spanwise direction, giving physical dimensions of approximately $1600\ \mathrm{mm} \times 1000\ \mathrm{mm} \times 500\ \mathrm{mm}$. The domain was selected to limit boundary influence while retaining feasible computational cost. It was not intended to reproduce the wind-tunnel wall confinement. The upstream plane was set as a velocity inlet, with the freestream speed determined by the target Reynolds number. The downstream

plane was set as a zero-gauge-pressure outlet. The top, bottom, and spanwise side boundaries were treated as slip walls to approximate far-field behaviour within a finite domain, and all wing surfaces were treated as no-slip walls.

Periodic and symmetry boundary conditions were not used. Although these would reduce computational cost, they would suppress spanwise flow structures and end effects as well as being difficult to experimentally verify. The angle of attack was applied by rotating the wing section about the quarter chord rather than by changing the freestream direction. This allowed the wake-refinement region to remain aligned with the model and avoided excessive refinement of unused domain regions across the angle-of-attack range.

The mesh was generated as a hybrid unstructured mesh, predominantly a poly-hexcore volume mesh. Curvature- and proximity-based local sizing was applied to the serrated leading edge so that the mesh resolution adapted to both fine and coarse serration geometries. The final surface sizing used a minimum cell size of approximately $0.05\ \mathrm{mm}$ and a maximum cell size of approximately $0.5\ \mathrm{mm}$ on the wing surface. A local wake-refinement region was defined around and downstream of the wing section, extending approximately $0.5C$ upstream, $6C$ downstream, $\pm 2C$ vertically, and $\pm C$ spanwise from the model. The wake-region cell size was set to approximately $1\ \mathrm{mm}$, or $0.01C$, to resolve the separated wake and unsteady flow features associated with the serrated leading edge.

A 30-layer boundary-layer mesh was applied to the wing surfaces. The first-layer height was adjusted as a function of Reynolds number to target $y^+ < 1$ for the large-eddy simulation cases, with first-layer heights of approximately $0.005\ \mathrm{mm}$ at $Re = 1 \times 10^5$ and $0.001\ \mathrm{mm}$ at $Re = 5 \times 10^5$. The final volume mesh varied with the serration geometry and angle of attack, with typical cell counts ranging from approximately 4×10^6 to 15×10^6 cells.

Table 2 – Computational setup summary.

Parameter	Value
Software	ANSYS Workbench / Fluent
Computational model	Large-eddy simulation (LES)
Automation	Python case generation, submission, and processing
Computing resources	UNSW Katana and NCI GADI
Vertical domain extent	$\pm 5C$
Upstream domain extent	$4C$
Downstream domain extent	$12C$
Spanwise domain extent	$\pm 2.5C$
Inlet boundary	Velocity inlet
Outlet boundary	Pressure outlet
Outer boundaries	Slip walls
Wing surfaces	No-slip walls
Angle-of-attack method	Wing rotation about quarter chord, α
Mesh type	Hybrid unstructured / poly-hexcore
Surface refinement	Curvature and proximity controls
Surface sizing	0.05–$0.5\ \mathrm{mm}$
Wake refinement size	$1\ \mathrm{mm}$, or $0.01C$
Boundary-layer mesh	30 layers
Near-wall target	$y^+ < 1$
First-layer height, low Re	$0.005\ \mathrm{mm}$
First-layer height, high Re	$0.001\ \mathrm{mm}$
Cell-count range	4×10^6–15×10^6
Initial time stepping	200 steps, $CFL = 10$–50
Final time stepping	1000 steps, $CFL = 1$–5
Runtime per simulation	4–$12\ \mathrm{h}$
Total computational work	$\approx 550,000$ core-hours

Large-eddy simulation (LES) was selected because the study centres on unsteady separated-flow regimes in which steady RANS was not reliable in preliminary stall and post-stall cases. Preliminary steady RANS simulations were useful at low angles of attack but unreliable in the separated-flow regimes. Unsteady RANS improved convergence behaviour but did not reproduce the expected stall and post-stall trends with sufficient fidelity. Previous studies have shown that lower-order turbulence models can capture some force trends for tubercled wings, while scale-resolving simulations are better suited to unsteady separated-flow analysis [10,11,19]. LES was therefore used as the primary model for the parametric sweep. The transient pressure-based LES used the WALE subgrid-scale model ($C_{\mathrm{WALE}} = 0.325$) with Kader near-wall blending, SIMPLE pressure–velocity coupling, second-order pressure discretisation, bounded central differencing for momentum, and bounded second-order implicit time integration.

A two-stage time-stepping approach was used to reduce computational cost while still resolving the final unsteady flow field. Each case was first advanced using a larger time step corresponding approximately to a Courant–Friedrichs–Lewy number of $CFL = 10$–50 for 200 time steps. This stage moved the solution through the initial transient. The time step was then reduced to approximately $CFL = 1$–5 for a further 1000 time steps to resolve the final unsteady force histories used for coefficient calculation. Aerodynamic coefficients were obtained by time averaging the converged portion of the final low-CFL stage. Each simulation required approximately 4–12 hours on 48-core cluster nodes, depending on mesh size and flow condition. Across data collection and setup development, the final two-Reynolds-number investigation required approximately $550,000$ core-hours.

2.3.1 Computational uncertainty

Finite-time sampling uncertainty in each time-averaged aerodynamic coefficient was estimated using the autocorrelation-aware autoregressive procedure of Oliver et al. [21], with uncertainty reported as a two-sided 95% uncertainty interval. Three spatial-resolution levels were used for representative mesh-sensitivity cases. Sensitivity to the averaging interval was assessed using nested windows comprising the final 400, 600, and 800 low-CFL time steps, with the final 600 steps used as the primary averaging interval. Joint coefficient uncertainties were propagated into C_L/C_D and the normalised performance ratios using correlation-preserving Monte Carlo sampling with 100,000 realisations. At the experimentally tested $Re = 1 \times 10^5$ conditions, the resulting simulation uncertainty was combined with simulation-input and experimental uncertainties following ASME V&V 20 [22], and the model-discrepancy interval was evaluated from the computational-experimental comparison error. At $Re = 5 \times 10^5$, model-form uncertainty was represented using a symmetric, regime-matched envelope equal to the largest absolute computational–experimental discrepancy observed at $Re = 1 \times 10^5$. This extrapolation is an assumption rather than a validated uncertainty and should therefore be interpreted as an approximate sensitivity bound. Representative mesh-resolution, domain-extent, and averaging-window checks did not alter the qualitative aerodynamic trends or the conclusions drawn from the parameter sweep.

The computational setup was designed to provide consistent trend prediction across the large parameter space rather than individually converged predictions for every geometry. The quantified finite-time and discretisation uncertainties were non-negligible relative to some of the smaller differences between configurations, particularly near stall. The analysis therefore emphasises coherent trends across neighbouring geometries and operating regimes rather than isolated extrema, while individual coefficient values are interpreted within their uncertainty intervals and the limitations of the common mesh, domain, and turbulence model. References to maxima, minima, and percentages of cases above or below unity are therefore based on nominal coefficient values and do not imply statistically unique rankings.

2.4 Experimental verification method

Experimental verification was conducted in the UNSW Educational Wind Tunnel (EWT). The test section measured $30.48\ \mathrm{cm} \times 30.48\ \mathrm{cm} \times 60.96\ \mathrm{cm}$ and was equipped with a three-component sting balance. The balance allowed a maximum geometric angle of attack of 23°, so a custom offset mount was used to extend the usable range. The mount placed the model approximately $30\ \mathrm{mm}$ away

from the sting support and introduced a -5° offset, giving an effective maximum angle of attack of approximately 28°.

The verification experiments were conducted at $Re = 1 \times 10^5$, corresponding to $V = 14.61\ \mathrm{m\,s^{-1}}$ for the $100\ \mathrm{mm}$ chord. The projected blockage was approximately 6%–10% over the selected high-angle range, excluding airfoil-thickness and mounting contributions. No correction was applied; this unavoidable wind-tunnel constraint may have affected the measured forces, so the experiments are used for qualitative trend verification rather than absolute validation. The models were manufactured from PLA using additive manufacturing, with the print direction kept consistent in the streamwise direction across all tested cases. The same mounting arrangement was used for all models.

Three wing-section geometries were tested: the unserrated baseline, a lower-intensity serration case, and a higher-intensity serration case. The tested configurations were:

$$[0,\ 0,\ 0]_{\mathrm{SC}}, \qquad \left[\frac{1}{20},\ 0.01,\ 0.35\right]_{\mathrm{SC}}, \qquad \left[\frac{1}{4},\ 0.075,\ 0.35\right]_{\mathrm{SC}}, \tag{6}$$

where $[w,a,t]_{\mathrm{SC}}$ denotes a serration combination. The angle-of-attack sweep used coarser increments away from stall and finer increments of approximately 0.5° through the stall region. Force data were acquired for 10 seconds at 100 Hz, giving a 1000-point average for each operating condition. The sting-balance normal and axial force measurements were transformed into lift and drag using the effective angle of attack, including the mount offset. Experimental uncertainty was estimated for each tested condition and incorporated into the computational–experimental uncertainty comparison.

The experiments were not intended to reproduce the full computational parameter sweep. Their purpose was to verify that the computational setup captured the main aerodynamic trends and relative behaviour of the baseline, low-intensity serration, and high-intensity serration cases. The experimental comparison was therefore used to support the selection of representative angles of attack and to provide confidence in the trend-based interpretation of the computational parameter study.

3. Results and Discussion

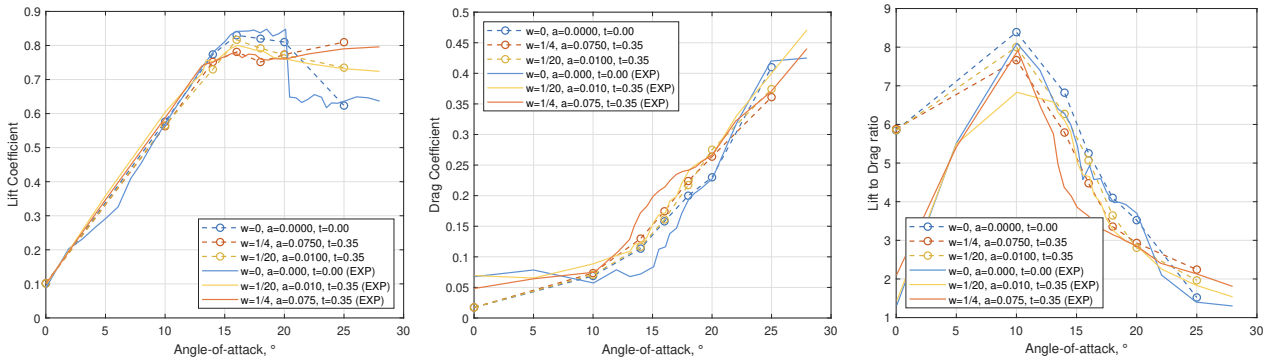
3.1 Experimental verification and stall-regime selection

Experimental verification was used to assess whether the computational setup captured the main aerodynamic trends required for the parametric study. The comparison was performed at $Re = 1 \times 10^5$ using three representative wing sections: the unserrated baseline, $[0,0,0]_{\mathrm{SC}}$; a low-intensity serration case, $[1/20,0.01,0.35]_{\mathrm{SC}}$; and a high-intensity serration case, $[1/4,0.075,0.35]_{\mathrm{SC}}$. The corresponding lift, drag, and lift-to-drag ratio comparisons are given in Figures 3a, 3b, and 3c, respectively.

The lift comparison shows the best agreement between the computational and experimental results. In Figure 3a, the CFD captures the overall lift-curve shape for all three models, including the sharper post-stall reduction in the unserrated wing section and the softer high-angle response in the serrated cases. The serrated cases show similar lift trends to the experiments at the main simulated angles of attack. The baseline lift curve is also captured well through the main stall region, although the exact stall transition and post-stall shape are not identical. The agreement supports comparative trend analysis across the serration geometries, but not exact prediction of every detail of the stall profile.

The drag comparison in Figure 3b shows the main limitation of the computational model. At a very low angle of attack, the CFD substantially underpredicts drag for all three models. At $\alpha = 0^\circ$, the CFD values are $C_D = 0.017$, while the experimental values range from 0.048 to 0.069, depending on the model. This corresponds to an underprediction of roughly 60%–75%. The discrepancy is most significant in the low-angle attached-flow region and is likely influenced by experimental surface roughness, model manufacturing, support effects, and tunnel conditions that are not fully represented in the simulation. The agreement improves as the flow approaches and passes through stall; from approximately $\alpha = 18^\circ$–20° onward, the CFD and experimental drag trends are much closer.

The effect of the drag discrepancy is most visible in Figure 3c. At low α, the underestimated drag leads to an overprediction of the computational C_L/C_D. At $\alpha = 0^\circ$, the computational C_L/C_D values are 2.8–4.4 times larger than the experimental values, depending on the model. This prevents the low-angle attached-flow region from being used as a reliable absolute validation of efficiency. However, the agreement improves across the stall and post-stall ranges, where the drag values converge and



(a) (b) (c)

Figure 3 – Experimental and computational stall profiles for the three tested models: (a) C_L, (b) C_D, and (c) C_L/C_D.

the computed C_L/C_D trend more closely matches the experimental behaviour. The verification should therefore be interpreted as trend verification for the separated-flow regimes used in the parametric study, not as full validation of absolute drag or efficiency over the entire range.

Based on this comparison, angles below approximately $\alpha = 15^\circ$ were not used for the main parametric study. The selected low-Reynolds-number operating points were $\alpha = 16^\circ$, 20°, and 25°, corresponding to representative pre-stall, stall, and post-stall conditions, respectively. These angles lie in the range where the CFD captures the main experimental trends while still separating the three aerodynamic regimes required for the wavelength–amplitude and termination-distance studies. The experimental verification was performed only for selected representative geometries, so it does not validate every case in the full computational sweep. Its purpose is to support the use of the computational model for comparative parametric analysis at $Re = 1 \times 10^5$.

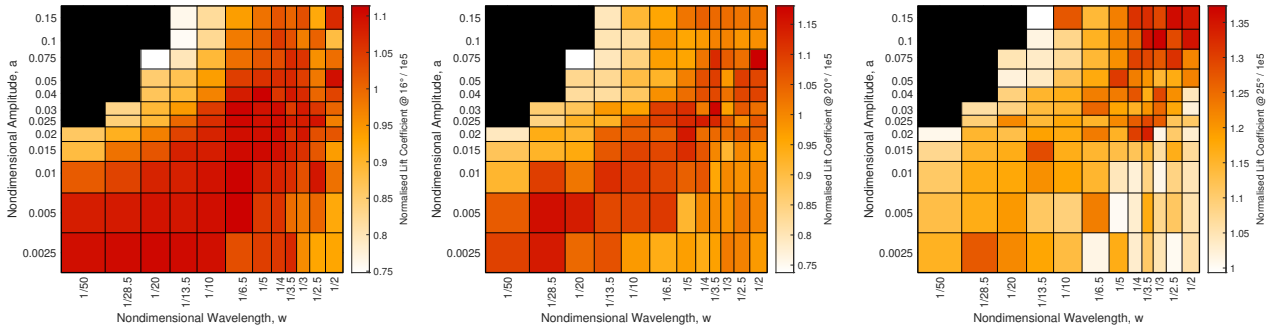
3.2 Wavelength–amplitude trends at $Re = 1 \times 10^5$

The first wavelength–amplitude sweep was performed at a fixed termination distance of $t = 0.35$. Serration combinations are denoted by $[w,a,t]_{\mathrm{SC}}$, and the coefficient values are given relative to the corresponding unserrated wing section at the same angle of attack. Values greater than unity therefore indicate an increase in $C_L/C_{L,0}$, $C_M/C_{M,0}$, or $(C_L/C_D)/(C_L/C_D)_0$, while values below unity indicate a reduction in $C_D/C_{D,0}$. The black regions in the wavelength–amplitude maps correspond to omitted serration combinations that were not included in the simulated parameter space.

At $\alpha = 16^\circ$, the pre-stall response is dominated by drag reduction rather than by a large increase in lift. The lift map in Figure 4a shows a broad region of moderate improvement, with 66.2% of the simulated combinations giving $C_L/C_{L,0} > 1$. The maximum lift ratio is $1.114\,[1.051, 1.181]$ at $[1/5, 0.04, 0.35]_{\mathrm{SC}}$, although several neighbouring combinations around $w/a = 5$–20 give similar lift values. The drag response is more decisive. As shown in Figure 5a, almost all simulated serration combinations reduce drag relative to the baseline, with the minimum value $C_D/C_{D,0} = 0.626\,[0.589, 0.665]$ occurring at $[1/13.5, 0.005, 0.35]_{\mathrm{SC}}$. The corresponding lift-to-drag map in Figure 6a therefore follows the drag trend more strongly than the lift trend. The maximum value of $(C_L/C_D)/(C_L/C_D)_0$ is $1.741\,[1.604, 1.882]$ at $[1/28.5, 0.0025, 0.35]_{\mathrm{SC}}$, with $[1/20, 0.0025, 0.35]_{\mathrm{SC}}$ giving an almost identical value.

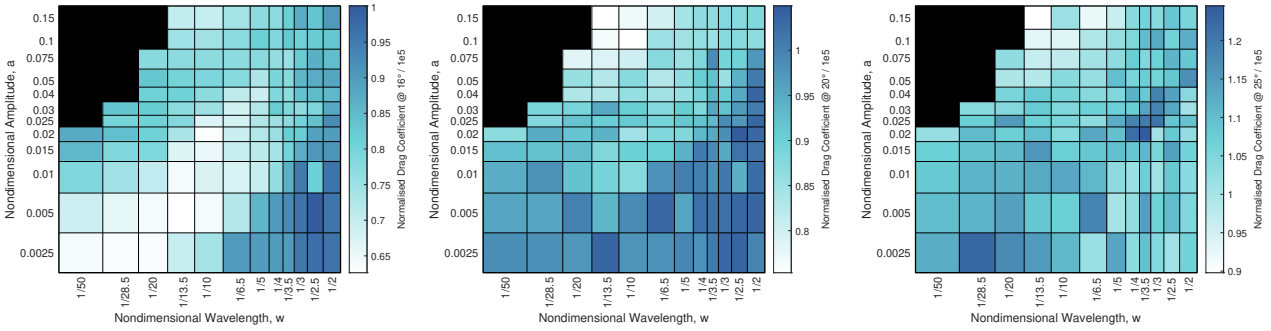
The w/a projections in Figures 8a, 9a, and 10a show that the pre-stall high-performing region is broad rather than sharply optimised. The top lift-to-drag combinations fall mostly between $w/a = 5$ and 20, with amplitudes no larger than approximately $a = 0.03$–0.04. This indicates that the pre-stall benefit, where present, comes from relatively low-amplitude serrations that perturb the attached flow only weakly. The scatter at repeated or similar w/a values also shows that w/a alone is insufficient to describe the response; amplitude and wavelength still affect the result independently.

At $\alpha = 20^\circ$, the stall-regime maps become more selective. The lift response in Figure 4b retains the same general preference for moderate w/a, but the high-performing region is narrower than at $\alpha = 16^\circ$. The maximum lift ratio is $1.181\,[1.081, 1.284]$ at $[1/2, 0.075, 0.35]_{\mathrm{SC}}$, while several of the strongest lift cases occur around $w/a = 5$–10. The drag map in Figure 5b shows a different trend from the



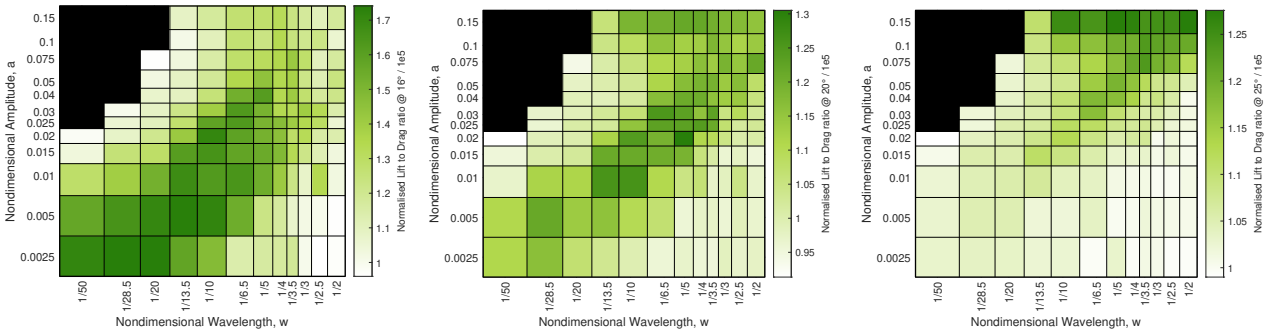
(a) (b) (c)

Figure 4 – Log-log wavelength–amplitude maps of normalised lift coefficient, $C_L/C_{L,0}$, at $\mathrm{Re} = 1 \times 10^5$ for the regimes (a) pre-stall ($\alpha = 16°$, $C_{L,0} = 0.760\,[0.730, 0.789]$), (b) stall ($\alpha = 20°$, $C_{L,0} = 0.755\,[0.713, 0.797]$), and (c) post-stall ($\alpha = 25°$, $C_{L,0} = 0.624\,[0.578, 0.669]$).



(a) (b) (c)

Figure 5 – Log-log wavelength–amplitude maps of normalised drag coefficient, $C_D/C_{D,0}$, at $\mathrm{Re} = 1 \times 10^5$ for the regimes (a) pre-stall ($\alpha = 16°$, $C_{D,0} = 0.229\,[0.219, 0.239]$), (b) stall ($\alpha = 20°$, $C_{D,0} = 0.300\,[0.280, 0.320]$), and (c) post-stall ($\alpha = 25°$, $C_{D,0} = 0.335\,[0.309, 0.361]$).

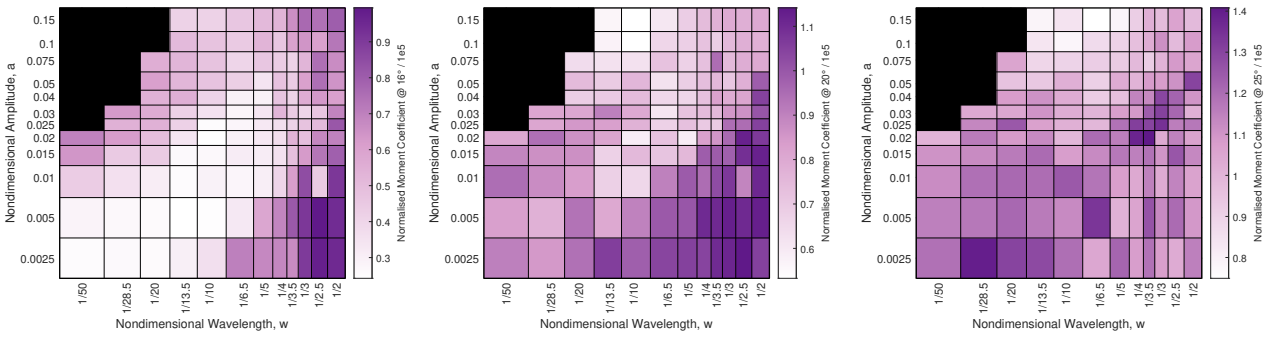


(a) (b) (c)

Figure 6 – Log-log wavelength–amplitude maps of normalised lift-to-drag ratio, $(C_L/C_D)/(C_L/C_D)_0$, at $\mathrm{Re} = 1 \times 10^5$ for the regimes (a) pre-stall ($\alpha = 16°$, $(C_L/C_D)_0 = 3.32\,[3.13, 3.51]$), (b) stall ($\alpha = 20°$, $(C_L/C_D)_0 = 2.52\,[2.32, 2.72]$), and (c) post-stall ($\alpha = 25°$, $(C_L/C_D)_0 = 1.86\,[1.74, 1.98]$).

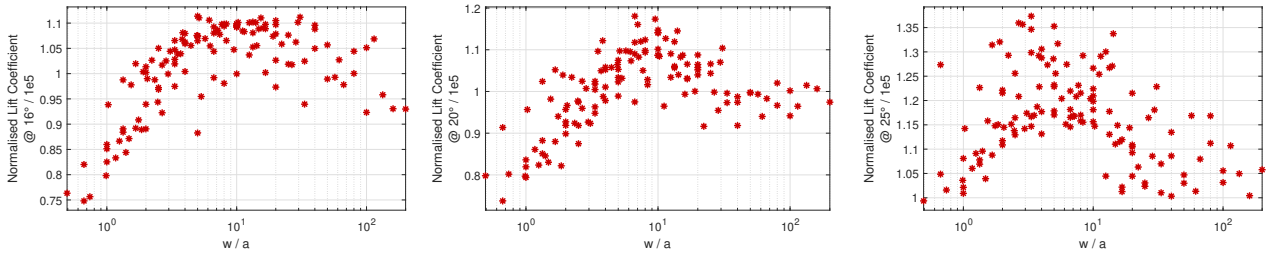
pre-stall case. The lowest drag values occur for larger-amplitude, low-w/a combinations, with the minimum value $C_D/C_{D,0} = 0.753\,[0.687, 0.820]$ at $[1/13.5, 0.15, 0.35]_{\mathrm{SC}}$. However, these low-drag cases do not all correspond to the best overall lift-to-drag ratios.

The combined performance at $\alpha = 20°$ is shown in Figure 6b. The maximum value of $(C_L/C_D)/(C_L/C_D)_0$ is $1.305\,[1.162, 1.450]$ at $[1/5, 0.02, 0.35]_{\mathrm{SC}}$. The strongest cases cluster around $w/a = 5$–10, including $[1/10, 0.01, 0.35]_{\mathrm{SC}}$, $[1/13.5, 0.01, 0.35]_{\mathrm{SC}}$, and $[1/6.5, 0.03, 0.35]_{\mathrm{SC}}$. The latter gives $(C_L/C_D)/(C_L/C_D)_0 = 1.253\,[1.121, 1.389]$, placing it among the better-performing cases. The favourable region is narrower than before stall and more sensitive to the balance between parameters.



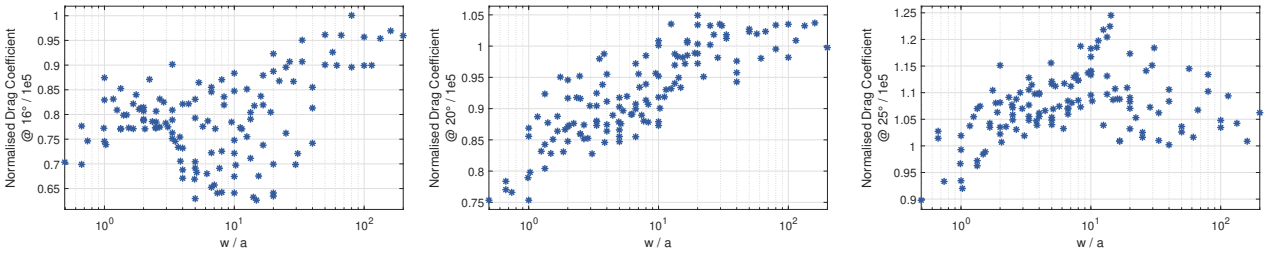
(a) (b) (c)

Figure 7 – Log-log wavelength–amplitude maps of normalised pitching-moment coefficient, $C_M/C_{M,0}$, at $\mathrm{Re} = 1 \times 10^5$ for the regimes (a) pre-stall ($\alpha = 16°$, $C_{M,0} = 0.116\,[0.106, 0.126]$), (b) stall ($\alpha = 20°$, $C_{M,0} = 0.123\,[0.110, 0.135]$), and (c) post-stall ($\alpha = 25°$, $C_{M,0} = 0.108\,[0.096, 0.120]$).



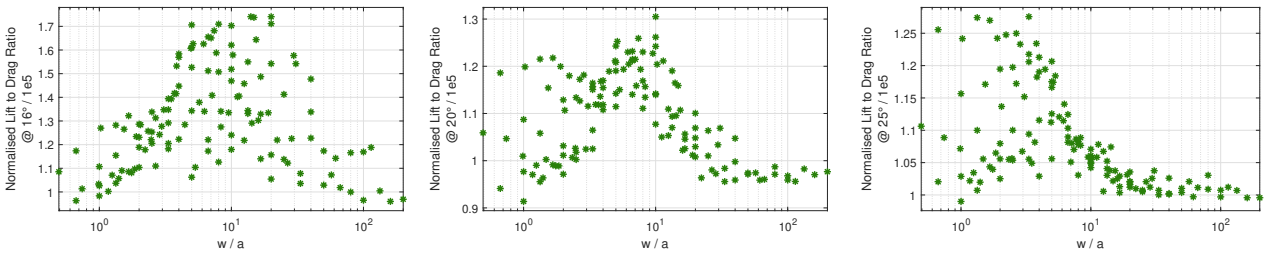
(a) (b) (c)

Figure 8 – Semi-log plots of the geometric ratio w/a against normalised lift, $C_L/C_{L,0}$, at $\mathrm{Re} = 1 \times 10^5$ for the regimes (a) pre-stall ($\alpha = 16°$, $C_{L,0} = 0.760\,[0.730, 0.789]$), (b) stall ($\alpha = 20°$, $C_{L,0} = 0.755\,[0.713, 0.797]$), and (c) post-stall ($\alpha = 25°$, $C_{L,0} = 0.624\,[0.578, 0.669]$).



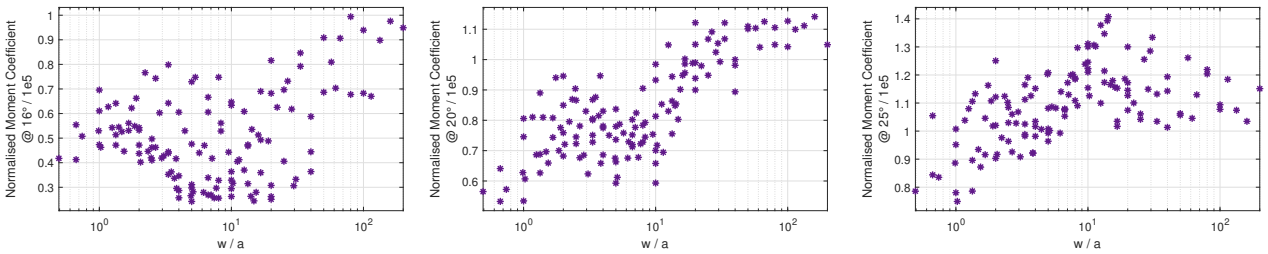
(a) (b) (c)

Figure 9 – Semi-log plots of the geometric ratio w/a against normalised drag, $C_D/C_{D,0}$, at $\mathrm{Re} = 1 \times 10^5$ for the regimes (a) pre-stall ($\alpha = 16°$, $C_{D,0} = 0.229\,[0.219, 0.239]$), (b) stall ($\alpha = 20°$, $C_{D,0} = 0.300\,[0.280, 0.320]$), and (c) post-stall ($\alpha = 25°$, $C_{D,0} = 0.335\,[0.309, 0.361]$).



(a) (b) (c)

Figure 10 – Semi-log plots of the geometric ratio w/a against normalised lift-to-drag ratio, $(C_L/C_D)/(C_L/C_D)_0$, at $\mathrm{Re} = 1 \times 10^5$ for the regimes (a) pre-stall ($\alpha = 16°$, $(C_L/C_D)_0 = 3.32\,[3.13, 3.51]$), (b) stall ($\alpha = 20°$, $(C_L/C_D)_0 = 2.52\,[2.32, 2.72]$), and (c) post-stall ($\alpha = 25°$, $(C_L/C_D)_0 = 1.86\,[1.74, 1.98]$).



(a) (b) (c)

Figure 11 – Semi-log plots of the geometric ratio w/a against normalised moment, $C_M/C_{M,0}$, at $\mathrm{Re} = 1 \times 10^5$ for the regimes (a) pre-stall ($\alpha = 16°$, $C_{M,0} = 0.116\,[0.106, 0.126]$), (b) stall ($\alpha = 20°$, $C_{M,0} = 0.123\,[0.110, 0.135]$), and (c) post-stall ($\alpha = 25°$, $C_{M,0} = 0.108\,[0.096, 0.120]$).

The post-stall behaviour at $\alpha = 25°$ is different again. Figure 4c shows that almost all serrated cases increase lift relative to the unserrated wing section, with 96.2% of the simulated combinations giving $C_L/C_{L,0} > 1$. The maximum lift ratio is $1.373\,[1.260, 1.486]$ at $[1/3, 0.1, 0.35]_{\mathrm{SC}}$. In contrast, Figure 5c shows that drag increases for most combinations, with only 7.7% of the simulated combinations yielding $C_D/C_{D,0} < 1$. The post-stall improvement in C_L/C_D is therefore lift-dominated rather than drag-dominated.

The lift-to-drag map in Figure 6c shows that the strongest post-stall cases are concentrated at the largest amplitudes. The maximum value of $(C_L/C_D)/(C_L/C_D)_0$ is $1.276\,[1.156, 1.398]$ at $[1/2, 0.15, 0.35]_{\mathrm{SC}}$, while $[1/5, 0.15, 0.35]_{\mathrm{SC}}$ gives a nearly identical value of $1.274\,[1.158, 1.392]$. The top-performing region is therefore not centred on the same w/a range as the pre-stall and stall cases; it is primarily an amplitude-driven region with $a = 0.075$–0.15 and $w/a \lesssim 5$. This is consistent with the interpretation that larger serrations are more effective once the baseline wing section is already separated or nearly fully separated, even though they may impose larger drag penalties outside the post-stall regime.

The w/a trend at $Re = 1 \times 10^5$ is regime-dependent. The nominal lift-to-drag optima occur at $w/a = 14.04$, 10.00, and 3.33 in the pre-stall, stall, and post-stall regimes, respectively. Despite this shift, the common band $w/a \approx 4$–8 contains at least one configuration within 5% of the nominal regime maximum at each of the three operating points. The configuration $[1/6.5, 0.03, 0.35]_{\mathrm{SC}}$, for which $w/a = 5.13$, is one of the strongest low-Re cross-regime compromises identified, remaining within 8% of the nominal regime maximum at all three operating points. This case gives $(C_L/C_D)/(C_L/C_D)_0 = 1.627\,[1.495, 1.766]$ at $\alpha = 16°$, $1.253\,[1.121, 1.389]$ at $\alpha = 20°$, and $1.174\,[1.069, 1.282]$ at $\alpha = 25°$. The scatter in Figures 10a, 10b, and 10c nevertheless shows that w/a does not uniquely determine performance, because wavelength and amplitude remain independently influential.

The moment-coefficient maps in Figures 7a, 7b, and 7c, with corresponding w/a trends in Figures 11a, 11b, and 11c, confirm that the serrations also alter the pitching-moment response. The trend is less useful as an independent performance metric in this section. At $\alpha = 16°$, all simulated cases reduce $C_M/C_{M,0}$, whereas the stall and post-stall cases exhibit a broader, more geometry-dependent spread. These results should be considered in any final design selection, but the wavelength–amplitude trends are governed primarily by the combined lift and drag response.

Overall, the low-Reynolds-number wavelength–amplitude sweep shows that the preferred serration geometry changes strongly with stall regime. The pre-stall response favours small, low-perturbation serrations and is largely drag-driven. The stall response narrows the favourable design space and gives the clearest support for a moderate w/a trend. The post-stall response shifts toward large-amplitude serrations, in which lift recovery outweighs the increase in drag. A single universal optimum is therefore not supported. Instead, $[1/6.5, 0.03, 0.35]_{\mathrm{SC}}$ is best interpreted as a strong cross-regime compromise at $Re = 1 \times 10^5$, while larger-amplitude cases are preferred when post-stall performance is the primary design objective.

3.3 Termination-distance sensitivity at $Re = 1 \times 10^5$

The termination distance, t, controls the chordwise extent over which the serrated leading-edge geometry is inserted before returning to the unmodified airfoil section. The main wavelength–amplitude sweep used $t = 0.35$, so a reduced-scope termination-distance sweep was used to determine the value's effect on the observed low-Reynolds-number trends. Three representative serration combinations were considered: a large-amplitude case, $[1/3, 0.1, t]_{\mathrm{SC}}$; an intermediate case, $[1/5, 0.02, t]_{\mathrm{SC}}$; and a fine, low-amplitude case, $[1/20, 0.005, t]_{\mathrm{SC}}$. The corresponding C_L, C_D, and C_L/C_D trends are given in Figures 12a–12c, Figures 13a–13c, and Figures 14a–14c, respectively.

Across the three cases, the dominant result is that termination distance is less influential than wavelength and amplitude. This is most clearly demonstrated by the fine serration case, $[1/20, 0.005, t]_{\mathrm{SC}}$, for which the C_L and C_D curves in Figures 14a and 14b nearly collapse over much of the tested angle-of-attack range. The corresponding C_L/C_D curves in Figure 14c show only modest separation, with approximate spreads of 5.62–5.75 at $\alpha = 16^\circ$, 2.79–3.03 at $\alpha = 20^\circ$, and 1.89–1.98 at $\alpha = 25^\circ$. This limited spread indicates that, when the leading-edge perturbation is small, changing the insertion length does not substantially alter the aerodynamic response at $Re = 1 \times 10^5$.

The larger serration case shows why this conclusion should not be extended too far. For $[1/3, 0.1, t]_{\mathrm{SC}}$, the separation between termination distances is visibly larger, particularly in the lift response around the pre-stall and near-stall region in Figure 12a. At $\alpha = 16^\circ$, the C_L/C_D values in Figure 12c range from approximately 3.72 to 4.51, with larger values occurring at intermediate-to-longer termination distances. By $\alpha = 20^\circ$ and 25°, however, the spread reduces to approximately 2.80–2.90 and 2.26–2.33, respectively. The associated drag curves in Figure 12b also remain close enough that no simple drag-based optimum in t is evident. The large-amplitude case is therefore more sensitive to termination distance than the fine-serration case, but the effect remains variable and does not yield a clear post-stall optimum.

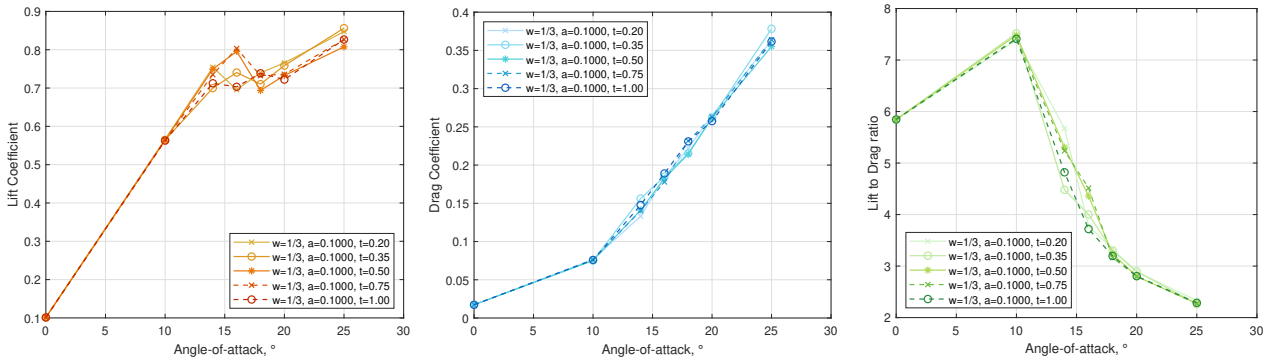
The intermediate case, $[1/5, 0.02, t]_{\mathrm{SC}}$, links these two behaviours. Its termination-distance sensitivity is larger than that of $[1/20, 0.005, t]_{\mathrm{SC}}$ in Figures 14a–14c, but less severe than that of $[1/3, 0.1, t]_{\mathrm{SC}}$ in Figures 12a–12c. In Figure 13c, the best values around $\alpha = 20^\circ$ occur for $t = 0.20$, 0.35, and 0.75, all of which are close to $C_L/C_D = 3.28$–3.29. In contrast, the shortest insertion, $t = 0.10$, is visibly weaker at the same angle, with $C_L/C_D \approx 2.86$. The lift and drag curves in Figures 13a and 13b indicate that this penalty is not caused by a single coefficient, but by the combined balance between lift retention and drag growth near stall. At $\alpha = 25^\circ$, the curves in Figure 13c again become closely grouped, with all termination distances lying near $C_L/C_D \approx 2.0$.

Taken together, Figures 12a–14c support treating t as a secondary design parameter at $Re = 1 \times 10^5$. Its influence increases with serration intensity and is most visible near the stall region, but it does not dominate the trends established by wavelength and amplitude. The use of $t = 0.35$ in the main wavelength–amplitude sweep is therefore reasonable. It is not a demonstrated optimum, but Figures 12c, 13c, and 14c show that it avoids the sharpest insertion case, performs comparably to neighbouring termination distances, and provides a representative partial-insertion geometry for the broader parameter study.

3.4 Wavelength–amplitude trends at $Re = 5 \times 10^5$

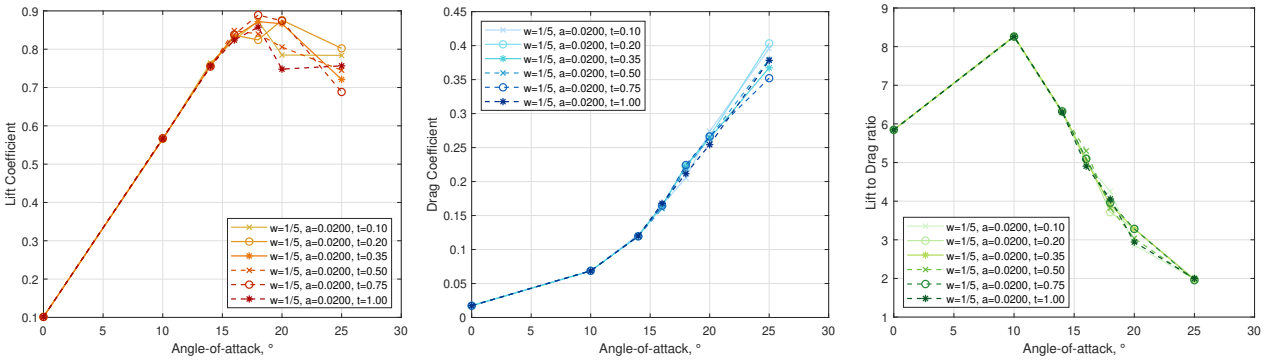
The high-Reynolds-number wavelength–amplitude sweep was performed at $Re = 5 \times 10^5$ and fixed termination distance $t = 0.35$. The representative angles of attack were selected computationally as $\alpha = 23^\circ$, 29°, and 34°, corresponding to pre-stall, stall, and post-stall operation for the high-Re baseline and representative serrated wing sections. The coefficient values are again presented relative to the corresponding unserrated wing section at the same angle of attack.

At $\alpha = 23^\circ$, the pre-stall response is more sharply divided than in the low-Re case. The lift map in Figure 15a shows that most serration combinations reduce lift relative to the baseline, with only 21.3% of the simulated combinations giving $C_L/C_{L,0} > 1$. The largest nominal lift ratio is $C_L/C_{L,0} = 1.023\,[0.955, 1.092]$ at $[1/20, 0.0025, 0.35]_{\mathrm{SC}}$, but its uncertainty interval spans unity, so a pre-stall lift increase is not resolved for this case. The high-lift region is concentrated at low amplitudes and moderate-to-large w/a, while larger-amplitude, low-w/a combinations produce substantial lift penalties.



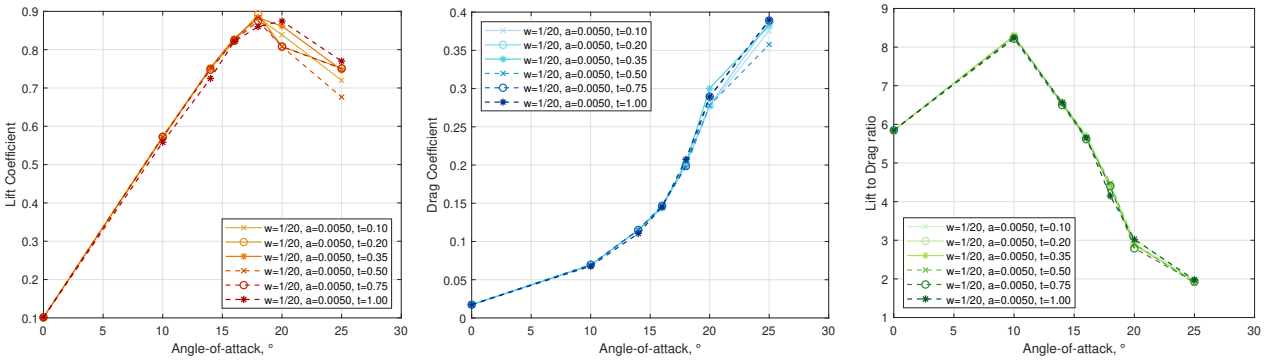
(a) (b) (c)

Figure 12 – Termination-distance sensitivity for $[1/3, 0.1, -]_{\mathrm{SC}}$ at $Re = 1 \times 10^5$: (a) C_L, (b) C_D, and (c) C_L/C_D.



(a) (b) (c)

Figure 13 – Termination-distance sensitivity for $[1/5, 0.02, -]_{\mathrm{SC}}$ at $Re = 1 \times 10^5$: (a) C_L, (b) C_D, and (c) C_L/C_D.



(a) (b) (c)

Figure 14 – Termination-distance sensitivity for $[1/20, 0.005, -]_{\mathrm{SC}}$ at $Re = 1 \times 10^5$: (a) C_L, (b) C_D, and (c) C_L/C_D.

The corresponding drag response in Figure 16a is mixed. The minimum drag ratio is $C_D/C_{D,0} = 0.899\,[0.844, 0.954]$ at $[1/10, 0.1, 0.35]_{\mathrm{SC}}$, but this case does not yield the best lift-to-drag performance due to its lift penalty. The w/a trend in Figure 20a shows a scattered response, with several low-drag cases at both low and moderate w/a. The combined result in Figure 17a is therefore governed by the balance between modest lift retention and drag reduction rather than by either coefficient alone.
The maximum nominal pre-stall value of $(C_L/C_D)/(C_L/C_D)_0$ is $1.055\,[0.959, 1.155]$ at $[1/20, 0.0025, 0.35]_{\mathrm{SC}}$. Its uncertainty interval spans unity, so this case is better interpreted as preserving baseline performance than as providing a resolved improvement. Only 28.3% of the nominal values exceed the baseline lift-to-drag ratio. The strongest cases are generally low-amplitude configurations with

$a \leq 0.02$ and w/a above approximately 8, with the highest values concentrated nearer $w/a = 20$–30. Figures 17a and 21a therefore show a pre-stall high-Re trend that is more selective than the low-Re pre-stall response. The favourable cases act mainly by minimising the penalty introduced by the serration geometry rather than by producing a large performance increase.

At $\alpha = 29°$, the stall-regime response is flatter in C_L/C_D but less favourable overall. Figure 15b shows that nearly all serration combinations reduce lift relative to the unserrated wing section. Only one case has a nominal value of $C_L/C_{L,0} > 1$, with $C_L/C_{L,0} = 1.009\,[0.952, 1.068]$ at $[1/2, 0.02, 0.35]_{\mathrm{SC}}$. Because the interval spans unity, this result indicates lift preservation rather than a resolved lift increase. The lift trend in Figure 19b increases with w/a over much of the data range, indicating that lower-amplitude, less disruptive serrations better preserve lift near stall at this Reynolds number.

The drag trend at $\alpha = 29°$ has the opposite character. Figure 16b shows that most serration combinations reduce drag relative to the baseline, with 97.6% of the simulated combinations giving $C_D/C_{D,0} < 1$. The minimum drag ratio is $0.747\,[0.698, 0.797]$ at $[1/6.5, 0.15, 0.35]_{\mathrm{SC}}$, with other low-drag cases occurring at relatively large amplitudes and low w/a. However, these same combinations generally incur lift losses, so the drag reduction does not translate directly into improved C_L/C_D.

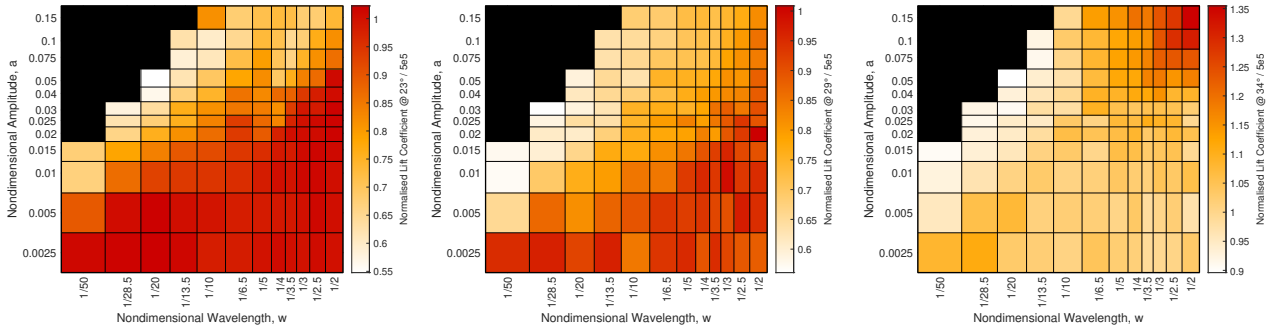
The lift-to-drag results in Figure 17b show that the stall case provides little improvement over the baseline. The maximum nominal value of $(C_L/C_D)/(C_L/C_D)_0$ is $1.050\,[0.958, 1.146]$ at $[1/28.5, 0.0025, 0.35]_{\mathrm{SC}}$, and this is the only nominal value above unity. Its uncertainty interval spans unity, so no stall-regime improvement in C_L/C_D is resolved. In contrast, the median value of $0.900\,[0.845, 0.956]$ remains below unity across its uncertainty interval, supporting a broad overall performance penalty. The w/a projection in Figure 21b shows a broad increase toward higher w/a, but the magnitude of the improvement remains small. The high-Re stall results therefore do not identify a distinct high-performing serration band comparable with the low-Re compromise region.

At $\alpha = 34°$, the post-stall response changes substantially. The lift map in Figure 15c shows that 75.6% of the simulated combinations increase lift relative to the baseline, with a maximum value of $C_L/C_{L,0} = 1.355\,[1.256, 1.456]$ at $[1/2, 0.15, 0.35]_{\mathrm{SC}}$. The strongest lift cases are concentrated at the largest amplitudes, particularly $a = 0.075$–0.15, and at moderate to large wavelengths. This is a different trend from the pre-stall and stall regimes, where lower-amplitude serrations were generally favoured.

The drag response in Figure 16c is less uniformly favourable. Many of the high-lift configurations also increase drag, with the largest drag ratio, $C_D/C_{D,0} = 1.148\,[1.063, 1.234]$, occurring at the same $[1/2, 0.15, 0.35]_{\mathrm{SC}}$ geometry that gives the maximum lift. The combined performance nevertheless improves for most configurations because the lift recovery outweighs the drag penalty. Figure 17c shows that 86.6% of the simulated combinations exceed the baseline lift-to-drag ratio.

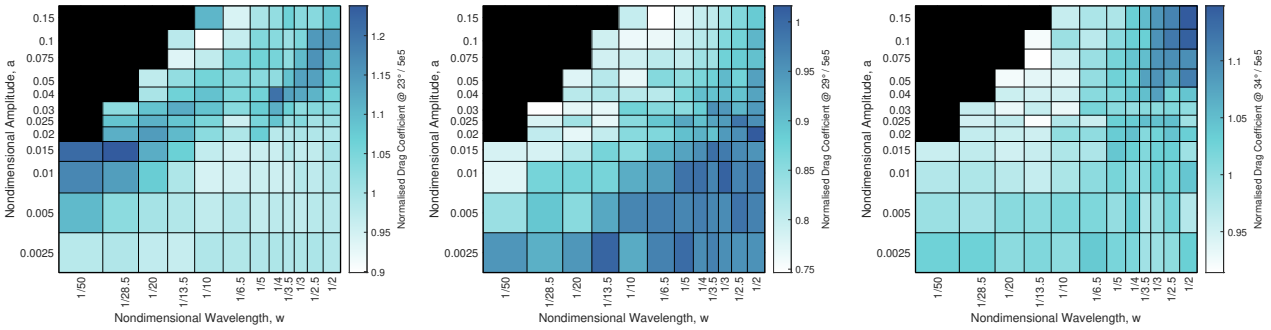
The maximum post-stall value of $(C_L/C_D)/(C_L/C_D)_0$ is $1.180\,[1.070, 1.292]$ at $[1/2, 0.15, 0.35]_{\mathrm{SC}}$, with $[1/5, 0.15, 0.35]_{\mathrm{SC}}$ close behind at $1.175\,[1.049, 1.302]$. The top-performing post-stall cases are concentrated at $a = 0.075$–0.15 and $w/a \approx 1$–6.7. The w/a trend in Figure 21c therefore differs from the pre-stall and stall cases: performance peaks at lower w/a because high amplitude becomes the dominant feature. The nominal post-stall optimum occurs at $w/a = 3.33$, compared with $w/a = 20.00$ and 14.04 in the high-Re pre-stall and stall regimes, respectively. Nevertheless, the shared screening band $w/a \approx 4$–8 contains configurations within 5% of the nominal maximum in all three high-Re regimes, with the upper end favoured before and near stall and the lower end favoured after stall.

The high-Re wavelength–amplitude sweep therefore shows a stronger regime dependence than the low-Re compromise trend. Low-amplitude, high-w/a serrations best preserve pre-stall and stall performance, but the magnitude of the improvement is small, and at stall, nearly all cases remain below the unserrated wing section in C_L/C_D. In contrast, the post-stall regime is clearly favourable to larger-amplitude serrations, where lift recovery dominates the aerodynamic response. The low-Re compromise geometry $[1/6.5, 0.03, 0.35]_{\mathrm{SC}}$ gives $(C_L/C_D)/(C_L/C_D)_0 = 0.822\,[0.750, 0.897]$, $0.888\,[0.814, 0.965]$, and $1.072\,[0.965, 1.180]$ at $\alpha = 23°$, $29°$, and $34°$, respectively. It therefore does not transfer directly as a high-Re optimum; although its post-stall value is nominally above unity, the uncertainty interval spans the baseline. For $Re = 5 \times 10^5$, the wavelength–amplitude selection is better interpreted as regime-specific: low-amplitude serrations minimise penalties before and near stall, while high-amplitude serrations are preferred when post-stall performance is the design priority.



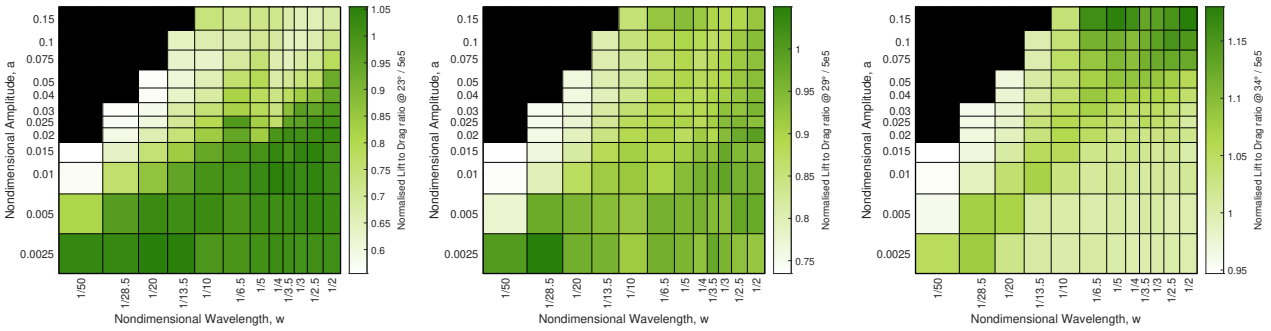
(a) (b) (c)

Figure 15 – Log-log wavelength–amplitude maps of normalised lift coefficient, $C_L/C_{L,0}$, at $\mathrm{Re} = 5 \times 10^5$ for the regimes (a) pre-stall ($\alpha = 23°$, $C_{L,0} = 1.11\,[1.05, 1.17]$), (b) stall ($\alpha = 29°$, $C_{L,0} = 1.13\,[1.09, 1.17]$), and (c) post-stall ($\alpha = 34°$, $C_{L,0} = 0.717\,[0.671, 0.764]$).



(a) (b) (c)

Figure 16 – Log-log wavelength–amplitude maps of normalised drag coefficient, $C_D/C_{D,0}$, at $\mathrm{Re} = 5 \times 10^5$ for the regimes (a) pre-stall ($\alpha = 23°$, $C_{D,0} = 0.292\,[0.276, 0.307]$), (b) stall ($\alpha = 29°$, $C_{D,0} = 0.510\,[0.483, 0.537]$), and (c) post-stall ($\alpha = 34°$, $C_{D,0} = 0.492\,[0.459, 0.526]$).



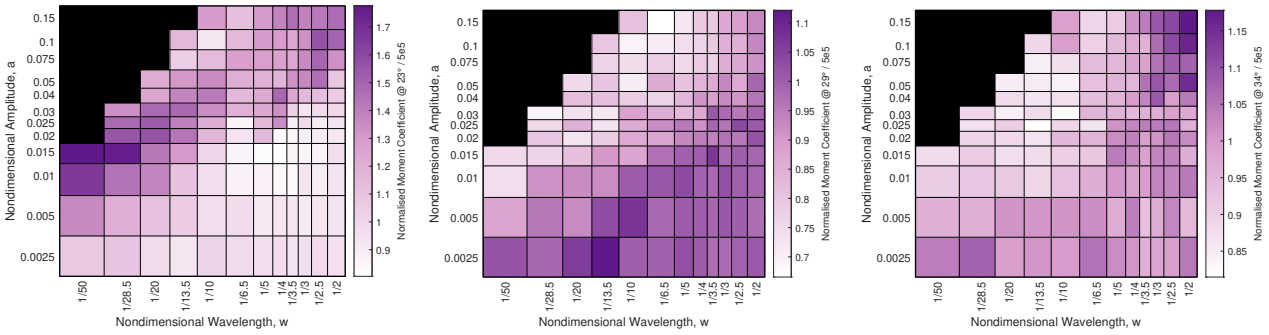
(a) (b) (c)

Figure 17 – Log-log wavelength–amplitude maps of normalised lift-to-drag ratio, $(C_L/C_D)/(C_L/C_D)_0$, at $\mathrm{Re} = 5 \times 10^5$ for the regimes (a) pre-stall ($\alpha = 23°$, $(C_L/C_D)_0 = 3.82\,[3.57, 4.07]$), (b) stall ($\alpha = 29°$, $(C_L/C_D)_0 = 2.21\,[2.08, 2.34]$), and (c) post-stall ($\alpha = 34°$, $(C_L/C_D)_0 = 1.46\,[1.34, 1.58]$).

The moment-coefficient results in Figures 18a, 18b, and 18c, with corresponding w/a trends in Figures 22a, 22b, and 22c, show that the serrations also affect pitching moment. The largest changes occur in the pre-stall case, while the post-stall moment trend partly follows the high-amplitude lift trend. These results are relevant for final design selection, but they do not change the main wavelength–amplitude interpretation, which is governed primarily by the lift and drag response.

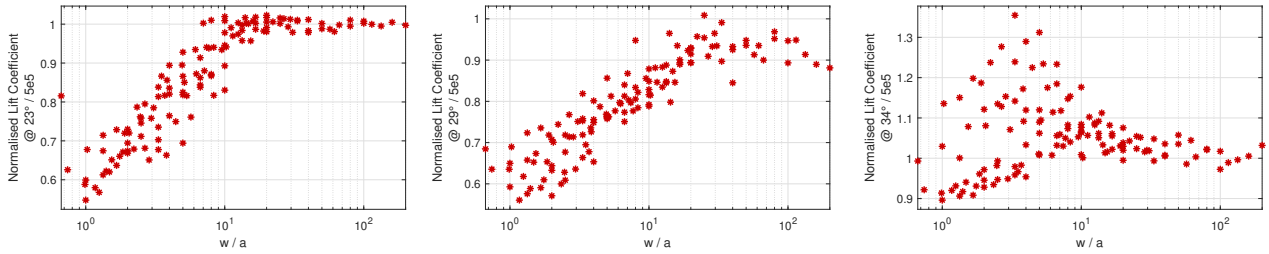
3.5 Termination-distance sensitivity at $Re = 5 \times 10^5$

The high-Reynolds-number termination-distance sweep was used to determine whether the fixed value $t = 0.35$ used in the main wavelength–amplitude investigation remains representative at $Re =$



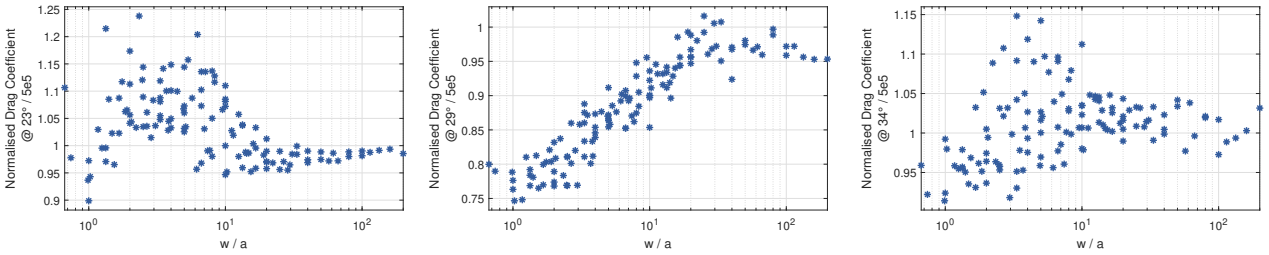
(a) (b) (c)

Figure 18 – Log-log wavelength–amplitude maps of normalised pitching-moment coefficient, $C_M/C_{M,0}$, at $\mathrm{Re} = 5 \times 10^5$ for the regimes (a) pre-stall ($\alpha = 23°$, $C_{M,0} = 0.0772\,[0.0719, 0.0826]$), (b) stall ($\alpha = 29°$, $C_{M,0} = 0.151\,[0.141, 0.160]$), and (c) post-stall ($\alpha = 34°$, $C_{M,0} = 0.132\,[0.121, 0.143]$).



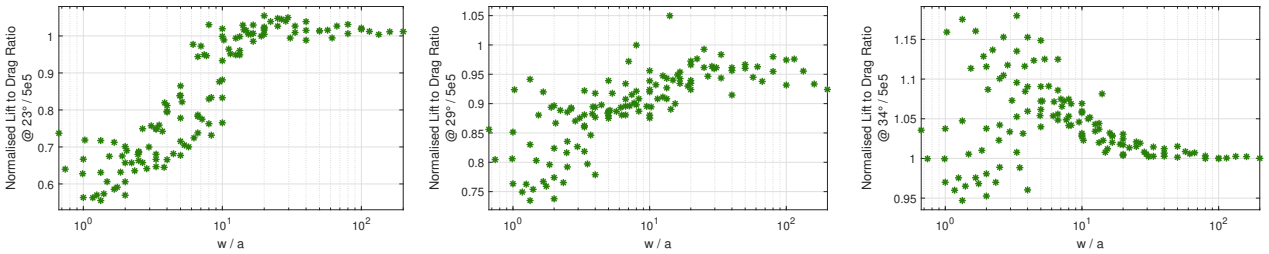
(a) (b) (c)

Figure 19 – Semi-log plots of the geometric ratio w/a against normalised lift, $C_L/C_{L,0}$, at $\mathrm{Re} = 5 \times 10^5$ for the regimes (a) pre-stall ($\alpha = 23°$, $C_{L,0} = 1.11\,[1.05, 1.17]$), (b) stall ($\alpha = 29°$, $C_{L,0} = 1.13\,[1.09, 1.17]$), and (c) post-stall ($\alpha = 34°$, $C_{L,0} = 0.717\,[0.671, 0.764]$).



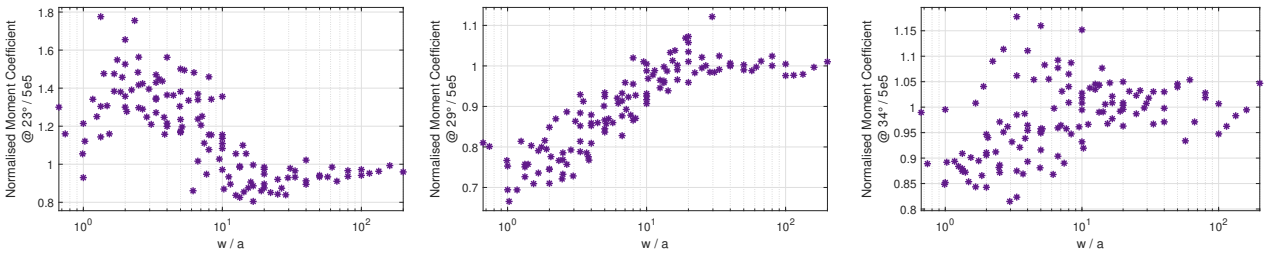
(a) (b) (c)

Figure 20 – Semi-log plots of the geometric ratio w/a against normalised drag, $C_D/C_{D,0}$, at $\mathrm{Re} = 5 \times 10^5$ for the regimes (a) pre-stall ($\alpha = 23°$, $C_{D,0} = 0.292\,[0.276, 0.307]$), (b) stall ($\alpha = 29°$, $C_{D,0} = 0.510\,[0.483, 0.537]$), and (c) post-stall ($\alpha = 34°$, $C_{D,0} = 0.492\,[0.459, 0.526]$).



(a) (b) (c)

Figure 21 – Semi-log plots of the geometric ratio w/a against normalised lift-to-drag ratio, $(C_L/C_D)/(C_L/C_D)_0$, at $\mathrm{Re} = 5 \times 10^5$ for the regimes (a) pre-stall ($\alpha = 23°$, $(C_L/C_D)_0 = 3.82\,[3.57, 4.07]$), (b) stall ($\alpha = 29°$, $(C_L/C_D)_0 = 2.21\,[2.08, 2.34]$), and (c) post-stall ($\alpha = 34°$, $(C_L/C_D)_0 = 1.46\,[1.34, 1.58]$).



(a) (b) (c)

Figure 22 – Semi-log plots of the geometric ratio w/a against normalised moment, $C_M/C_{M,0}$, at $\mathrm{Re} = 5\times10^5$ for the regimes (a) pre-stall ($\alpha = 23°$, $C_{M,0} = 0.0772\,[0.0719, 0.0826]$), (b) stall ($\alpha = 29°$, $C_{M,0} = 0.151\,[0.141, 0.160]$), and (c) post-stall ($\alpha = 34°$, $C_{M,0} = 0.132\,[0.121, 0.143]$).

5×10^5. The same three serration combinations were considered as in the low-Re termination study: $[1/3, 0.1, t]_{\mathrm{SC}}$, $[1/5, 0.02, t]_{\mathrm{SC}}$, and $[1/20, 0.005, t]_{\mathrm{SC}}$. Their corresponding C_L, C_D, and C_L/C_D trends are given in Figures 23a–23c, Figures 24a–24c, and Figures 25a–25c, respectively.

At $Re = 5\times10^5$, the termination distance is a secondary parameter compared with wavelength and amplitude. The large-amplitude case, $[1/3, 0.1, t]_{\mathrm{SC}}$, shows the weakest sensitivity. In Figure 23c, the C_L/C_D values vary only from approximately 2.47 to 2.50 at $\alpha = 23°$, 1.95 to 1.97 at $\alpha = 29°$, and 1.64 to 1.66 at $\alpha = 34°$. The lift and drag curves in Figures 23a and 23b show similarly small separations. No monotonic dependence on t is evident in this large-serration case.

The intermediate case, $[1/5, 0.02, t]_{\mathrm{SC}}$, gives the clearest termination-distance sensitivity. In Figure 24c, the approximate C_L/C_D values at $\alpha = 23°$ range from 2.98 for $t = 0.20$ to 3.39 for $t = 1.00$, with $t = 0.10$ also high at approximately 3.38. This indicates that the response is not simply improved by increasing insertion length. Instead, the sensitivity at this angle results from the combined balance of lift and drag in Figures 24a and 24b. At $\alpha = 29°$ and $34°$, the same case becomes much less sensitive to termination distance, with C_L/C_D ranges of approximately 1.92–1.98 and 1.49–1.50, respectively.

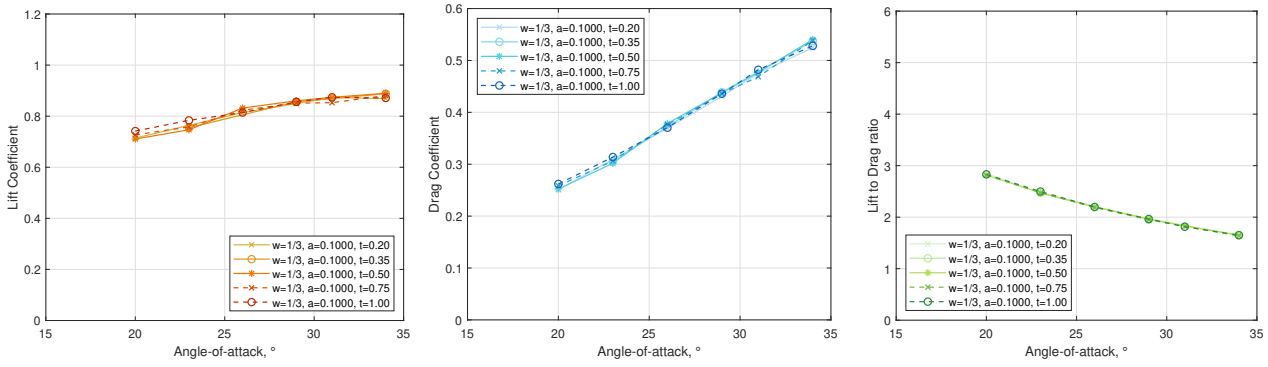
The fine serration case, $[1/20, 0.005, t]_{\mathrm{SC}}$, shows a mild preference for longer termination distances before stall. In Figure 25c, the C_L/C_D at $\alpha = 23°$ increases from approximately 3.69 at $t = 0.10$ to 3.97 at $t = 1.00$. This trend is consistent with the lift and drag behaviour in Figures 25a and 25b, but it weakens near and beyond stall. At $\alpha = 29°$ and $34°$, the C_L/C_D curves are again closely grouped, with approximate spreads of only 2.11–2.17 and 1.55–1.57.

Taken together, Figures 23a–25c show that high-Re termination-distance effects are weak and non-monotonic, and are most visible before or near stall. The results do not support a single optimum termination distance across the tested serration intensities or angles of attack. The use of $t = 0.35$ in the main wavelength–amplitude sweep is therefore justified as a representative partial-insertion value rather than as an optimum. It avoids the shortest-insertion case, remains within the clustered performance range under most conditions, and allows the main results to focus on the stronger effects of wavelength and amplitude.

3.6 Comparison across Reynolds numbers and design implications

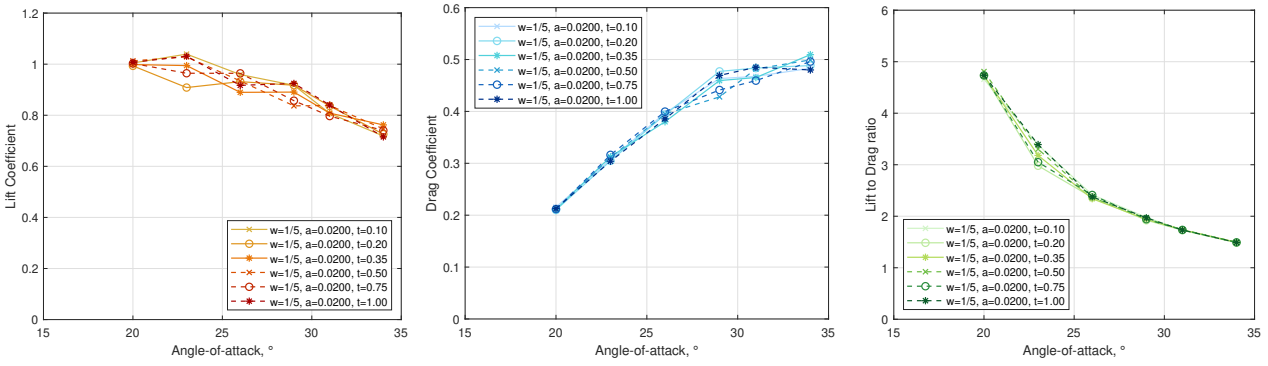
The combined results show that leading-edge serrations are best interpreted as regime-dependent stall-management devices rather than universal lift- or efficiency-enhancement devices. At $Re = 1\times10^5$, the three operating regimes still shared a recognisable compromise region. Low-to-moderate amplitudes and moderate wavelength-to-amplitude ratios were favoured before and near stall, while the post-stall response shifted toward larger amplitudes. The configuration $[1/6.5, 0.03, 0.35]_{\mathrm{SC}}$ was one of the strongest cross-regime compromises identified, with its nominal normalised C_L/C_D remaining within 8% of the regime maximum at $\alpha = 16°$, $20°$, and $25°$. It was not optimal in every regime, but retained post-stall benefit without incurring the largest pre-stall penalty.

At $Re = 5\times10^5$, this compromise behaviour weakened. The favoured low-Reynolds-number geometry did not transfer directly to the high-Reynolds-number pre-stall or stall cases, where lower-amplitude serrations better preserved performance. The strongest nominal high-Reynolds-number gains before



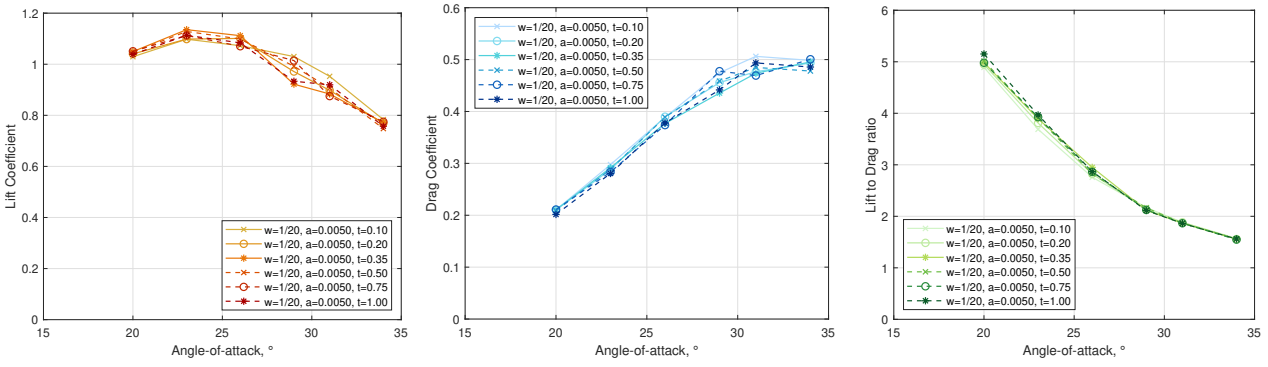
(a) (b) (c)

Figure 23 – Termination-distance sensitivity for $[1/3, 0.1, -]_{\mathrm{SC}}$ at $Re = 5 \times 10^5$: (a) C_L, (b) C_D, and (c) C_L/C_D.



(a) (b) (c)

Figure 24 – Termination-distance sensitivity for $[1/5, 0.02, -]_{\mathrm{SC}}$ at $Re = 5 \times 10^5$: (a) C_L, (b) C_D, and (c) C_L/C_D.



(a) (b) (c)

Figure 25 – Termination-distance sensitivity for $[1/20, 0.005, -]_{\mathrm{SC}}$ at $Re = 5 \times 10^5$: (a) C_L, (b) C_D, and (c) C_L/C_D.

and near stall were small and were not resolved from the baseline within their uncertainty intervals, while the post-stall case again showed a clear preference for larger-amplitude serrations. This indicates that increasing Re does not simply scale the low-Re optimum to a new operating condition. Instead, the preferred serration geometry becomes more dependent on the intended regime: low-amplitude serrations are the more conservative choice where pre-stall or near-stall efficiency must be preserved, while larger-amplitude serrations are more relevant when post-stall force retention is the primary objective.

For cross-regime comparison, a screening band was defined as the narrowest contiguous range of tested w/a values containing at least one configuration whose nominal normalised lift-to-drag ratio

was no less than 95% of the maximum value in each regime. The wavelength-to-amplitude ratio remains useful as a cross-regime screening variable, although it does not define a universal optimum. The nominal C_L/C_D optima occur at $w/a = 14.04$, 10.00, and 3.33 at $Re = 1 \times 10^5$, and at $w/a = 20.00$, 14.04, and 3.33 at $Re = 5 \times 10^5$, for the respective pre-stall, stall, and post-stall conditions. The preferred ratio therefore shifts from approximately 10–20 before and near stall to approximately 3–4 after stall. However, among the tested geometries, $w/a \approx 4$–8 is the narrowest contiguous interval containing at least one configuration within 5% of the nominal regime-specific maximum normalised lift-to-drag ratio at all six operating points. This range is best interpreted as a shared cross-regime screening band rather than as a universal optimum: the preferred position within it changes with stall regime, and wavelength and amplitude remain independently influential. This interpretation is consistent with previous studies showing that serration and tubercle performance depend strongly on geometry, airfoil profile, Reynolds number, and operating condition [3–5, 7, 8, 15].

The termination-distance sweeps carry relatively high finite-time uncertainty compared with many of the observed differences and should therefore be interpreted cautiously as broad qualitative trends rather than precise rankings. At both Reynolds numbers, changing t had a weaker effect than changing wavelength or amplitude. The influence of t was most visible near stall and for selected serration intensities, but no consistent optimum was evident. Very short insertion lengths could introduce local penalties, while longer insertions did not consistently improve performance. The value $t = 0.35$ used in the main wavelength–amplitude sweep is therefore justified as a representative partial-insertion geometry. It should not be interpreted as an optimal termination distance, but it is suitable for isolating the stronger effects of w and a.

From an application perspective, these results are most relevant to systems that repeatedly operate near stall, experience off-design incidence angles, or prioritise predictable stall behaviour over maximum attached-flow efficiency. UAVs and light aircraft are the most direct aerospace application class, because their operating Reynolds numbers and off-design conditions are closest to the present study. Training aircraft or other safety-sensitive light aircraft may also be relevant where softer stall behaviour is prioritised over cruise performance. For higher-performance or aerobatic aircraft, the concept is more plausible as a specialised high-α or manoeuvrability device than as a general aerodynamic upgrade. These aircraft-level implications should still be treated as design motivations rather than demonstrated full-aircraft outcomes [16, 18, 23].

The same stall-management framing extends to non-aircraft applications, but with increasing need for application-specific validation. Wind-turbine blades, propellers, rotors, fans, compressor cascades, hydrofoils, and rudders can all encounter off-design incidence or dynamic-stall conditions where stall margin, force retention, or load smoothing may be valuable. The most defensible industrial interpretation is therefore not that serrations improve peak efficiency, but that they may widen the usable incidence range or reduce the severity of flow-separation-driven force changes. Compressor and fan applications may be relevant to stall-margin improvement, whereas marine hydrofoils and rudders may be more relevant to unsteady load management than to increased lift [14, 24–26].

The present results do not support broad claims about cruise-optimised aircraft or universal low-angle benefit. A fixed serrated leading edge is present under all operating conditions, so any high-α benefit must be weighed against potential low-α drag, lift, manufacturing, contamination, and certification penalties. Selected studies report favourable low-angle or near-stall behaviour for particular geometries, but the present data support a more conservative conclusion: leading-edge serrations are most promising where stall tolerance, off-design robustness, or post-stall control are worth trading against possible attached-flow penalties. Final geometry selection should therefore be performed at the relevant operating Re and stall regime, rather than transferred directly from a low-Reynolds-number optimum or from a single value of w/a.

4. Conclusion

This paper investigated sinusoidal leading-edge serrations on a cambered NACA 2412 wing section with an aspect ratio of 2. Wavelength, amplitude, and termination distance were varied across pre-stall, stall, and post-stall regimes at $Re = 1 \times 10^5$ and $Re = 5 \times 10^5$. An automated LES workflow was used for the parameter study, with selected low-Reynolds-number cases experimentally verified.

At $Re = 1 \times 10^5$, performance depended strongly on stall regime. Smaller, lower-amplitude serrations were generally favoured before stall, whereas larger amplitudes became more favourable after stall, where lift recovery outweighed the drag increase in the strongest cases. The configuration $[1/6.5, 0.03, 0.35]_{\mathrm{SC}}$ was among the strongest low-Reynolds-number compromises, remaining within 8% of the nominal regime maximum at all three operating points.

At $Re = 5 \times 10^5$, the preferred geometry was more regime-specific. Low-amplitude, high-w/a serrations better preserved pre-stall and stall performance, while larger amplitudes were again favoured post-stall. The low-Reynolds-number compromise did not transfer directly, showing that serration geometry should be selected for the relevant Reynolds number and angle-of-attack range.

Across six operating points, the nominal optima shifted from $w/a \approx 10$–20 before and near stall to $w/a \approx 3.3$ after stall. Nevertheless, a shared screening band of $w/a \approx 4$–8 contained regime-specific configurations within 5% of each nominal maximum normalised lift-to-drag ratio. This band provides a useful initial screening range, but wavelength and amplitude remain independently influential. Termination distance was secondary within the tested space, supporting $t = 0.35$ as a representative partial-insertion geometry rather than an optimum.

The main practical output of this study is the combined dataset and performance maps. These provide an initial basis for industry-led, application-specific design, but not a transferable final geometry: performance remains sensitive to airfoil profile, planform, Reynolds number, and operating regime. Leading-edge serrations should therefore be treated as regime-dependent stall-management devices rather than general lift- or efficiency-enhancement devices. Further work should test the identified trends on additional airfoils, aspect ratios, Reynolds numbers, dynamic-stall conditions, and application-specific geometries.

5. Acknowledgements

I gratefully acknowledge the support of Professor Con Doolan for supervision and guidance throughout my work. The computational component of this study used the UNSW Compute Cluster Katana (DOI: 10.26190/669X-A286) and the National Computational Infrastructure GADI cluster. Generative AI assisted with language editing; all technical content was created by the author.

6. Contact Author Email Address

mailto: jordanjwhittaker@gmail.com

7. Copyright Statement

The authors confirm that they, and/or their company or organization, hold copyright on all of the original material included in this paper. The authors also confirm that they have obtained permission, from the copyright holder of any third party material included in this paper, to publish it as part of their paper. The authors confirm that they give permission, or have obtained permission from the copyright holder of this paper, for the publication and distribution of this paper as part of the ICAS proceedings or as individual off-prints from the proceedings.

References

[1] Fish FE and Battle JM. Hydrodynamic design of the humpback whale flipper. *Journal of Morphology*, Vol. 225, No. 1, pp 51–60, 1995.

[2] Miklosovic DS, Murray MM, Howle LE and Fish FE. Leading-edge tubercles delay stall on humpback whale (*Megaptera novaeangliae*) flippers. *Physics of Fluids*, Vol. 16, No. 5, pp L39–L42, 2004.

[3] Johari H, Henoch C, Custodio D and Levshin A. Effects of leading-edge protuberances on airfoil performance. *AIAA Journal*, Vol. 45, No. 11, pp 2634–2642, 2007.

[4] Hansen KL, Kelso RM and Dally BB. Performance variations of leading-edge tubercles for distinct airfoil profiles. *AIAA Journal*, Vol. 49, No. 1, pp 185–194, 2011.

[5] Hansen KL. *Effect of leading edge tubercles on airfoil performance*. PhD thesis, University of Adelaide, School of Mechanical Engineering, 2012.

[6] Fernandes I, Sapkota Y, Mammen T, Rasheed A, Rebello C and Kim YH. Theoretical and experimental investigation of leading edge tubercles on the wing performance. *Proc 2013 Aviation Technology, Integration, and Operations Conference*, Los Angeles, CA, AIAA Paper 2013-4300, 2013.

[7] Lacagnina G, Chaitanya P, Kim JH, Berk T, Joseph P, Choi KS, Ganapathisubramani B, Hasheminejad SM, Chong TP, Stalnov O, Shahab MF, Omidyeganeh M and Pinelli A. Leading edge serrations for the reduction of aerofoil self-noise at low angle of attack, pre-stall and post-stall conditions. *International Journal of Aeroacoustics*, Vol. 20, No. 1–2, pp 130–156, 2021.

[8] Stalnov O and Chong TP. Scaling of lift coefficient of an airfoil with leading-edge serrations. *AIAA Journal*, Vol. 57, No. 8, pp 3615–3619, 2019.

[9] Favier J, Pinelli A and Piomelli U. Control of the separated flow around an airfoil using a wavy leading edge inspired by humpback whale flippers. *Comptes Rendus Mecanique*, Vol. 340, No. 1–2, pp 107–114, 2012.

[10] Perez-Torro R and Kim JW. A large-eddy simulation on a deep-stalled aerofoil with a wavy leading edge. *Journal of Fluid Mechanics*, Vol. 813, pp 23–52, 2017.

[11] Liu K, Song B, Xue D, Yang W, Chen A and Wang Z. Numerical study of the aerodynamic effects of bio-inspired leading-edge serrations on a heaving wing at a low Reynolds number. *Aerospace Science and Technology*, Vol. 124, pp 107529, 2022.

[12] Rostamzadeh N, Kelso RM, Dally BB and Hansen KL. The effect of undulating leading-edge modifications on NACA 0021 airfoil characteristics. *Physics of Fluids*, Vol. 25, No. 11, pp 117101, 2013.

[13] Sathyabhama A and Sreejith BK. Numerical investigation on the effect of leading-edge tubercles on the laminar separation bubble. *Journal of Applied Fluid Mechanics*, Vol. 15, No. 3, pp 767–780, 2022.

[14] Joseph J and Sathyabhama A. Leading edge tubercle on wind turbine blade to mitigate problems of stall, hysteresis, and laminar separation bubble. *Energy Conversion and Management*, Vol. 255, pp 115337, 2022.

[15] Wang D, Cai C, Zha R, Peng C, Feng X, Liang P, Meng K, Kou J, Maeda T and Li Q. Impact of leading-edge tubercles on airfoil aerodynamic performance and flow patterns at different Reynolds numbers. *Energies*, Vol. 17, No. 21, pp 5518, 2024.

[16] Post ML, Decker R, Sapell AR and Hart JS. Effect of bio-inspired sinusoidal leading-edges on wings. *Aerospace Science and Technology*, Vol. 81, pp 128–140, 2018.

[17] Wei Z, Toh JWA, Ibrahim IH and Zhang Y. Aerodynamic characteristics and surface flow structures of moderate aspect-ratio leading-edge tubercled wings. *European Journal of Mechanics - B/Fluids*, Vol. 75, pp 143–152, 2019.

[18] Bardera R, Rodriguez-Sevillano AA, Barroso-Barderas E and Matias-Garcia JC. CFD study of the effect of leading-edge tubercles on the aerodynamic characteristics of a small UAV based on Eppler 186 airfoils. *Results in Engineering*, Vol. 23, pp 102639, 2024.

[19] Ali I, Hussain T, Unar IN, Kumar L and Ahad IU. Turbulence model study for aerodynamic analysis of the leading edge tubercle wing for low Reynolds number flows. *Heliyon*, Vol. 10, No. 11, pp e32148, 2024.

[20] Whittaker JJ and Doolan C. Parametric aerodynamic study of the properties of leading-edge serrations on wing sections. *Proc 2025 AIAA Regional Student Conferences*, University of Sydney, Sydney, Australia, AIAA Paper 2025-106570, 2025.

[21] Oliver TA, Malaya N, Ulerich R and Moser RD. Estimating uncertainties in statistics computed from direct numerical simulation. *Physics of Fluids*, Vol. 26, No. 3, pp 035101, 2014.

[22] ASME V&V 20 Committee. Standard for verification and validation in computational fluid dynamics and heat transfer. ASME V&V 20-2009 (R2021), American Society of Mechanical Engineers, New York, 2009.

[23] Sudhakar S, Karthikeyan N and Venkatakrishnan L. Influence of leading edge tubercles on aerodynamic characteristics of a high aspect-ratio UAV. *Aerospace Science and Technology*, Vol. 69, pp 281–289, 2017.

[24] Keerthi MC, Rajeshwaran MS, Kushari A and De A. Effect of leading-edge tubercles on compressor cascade performance. *AIAA Journal*, Vol. 54, No. 3, pp 912–923, 2016.

[25] Le Fouest S and Mulleners K. The dynamic stall dilemma for vertical-axis wind turbines. *Renewable Energy*, Vol. 198, pp 505–520, 2022.

[26] Ricard G, Jacobi G, Fiscaletti D and Buchner AJ. Dynamic stall of a hydrofoil with tubercles in surface gravity waves. *Journal of Fluid Mechanics*, Vol. 1028, pp A4, 2026.